

**FACULTY  
OF MATHEMATICS  
AND PHYSICS**  
Charles University

**MASTER THESIS**

Filip Novotný

**Measurements of Quantum Turbulence  
in Spherically Symmetric Counterflow**

Department of Low-Temperature Physics

Supervisor of the master thesis: doc. RNDr. David Schmoranzer,  
Ph.D.

Consultant: Mgr. Šimon Midlik

Study programme: Physics

Study branch: Physics of Condensed Matter and  
Materials

Prague 2022



I declare that I carried out this master thesis independently, and only with the cited sources, literature and other professional sources. It has not been used to obtain another or the same degree.

I understand that my work relates to the rights and obligations under the Act No. 121/2000 Sb., the Copyright Act, as amended, in particular the fact that the Charles University has the right to conclude a license agreement on the use of this work as a school work pursuant to Section 60 subsection 1 of the Copyright Act.

In ..... date .....

Author's signature



First of all, I would like to thank my supervisor, doc. David Schmoranzer, who led me through my master's study and helped me to plan, discuss, and perform measurements. Subsequently, he was willing to help with data processing and their interpretation. I am also thankful that he had never sent me away when I needed to discuss something, even though I could be sometimes annoying.

I also want to say a big thank Mgr. Šimon Midlik, who helped me directly with experimental and technical things, which would not be feasible without him. He learned and showed me a lot about the cryogenic experiment.

The other thank belongs to dr. Yunhu Huang and dr. Zhuolin Xie. They completely performed the measurement of the temperature profile when I could not be present in our laboratory due to Covid restrictions.

I should also mention prof. Ladislav Skrbek, the head of our group, who helped with the discussion of the results, and Ing. Bohumil Vejr, who manufactured the spherical cell.

And at the end, I thank my family, especially my mum, who always stood by me and always supported me whenever I lost my determination to finish this work.



Title: Measurements of Quantum Turbulence in Spherically Symmetric Counterflow

Author: Filip Novotný

Department: Department of Low-Temperature Physics

Supervisor: doc. RNDr. David Schmoranzler, Ph.D.

Consultant: Mgr. Šimon Midlik

Abstract: This work concerns with quantum turbulence in superfluid helium generated via spherically symmetric thermal counterflow. To this end, we designed a spherical brass cell with a point-like heater in the middle. The turbulence is detected using attenuation of second sound resonances. We mapped these resonances up to 10 kHz and compared them with theoretically calculated values. We obtained a dependence of Vortex line density (VLD) on the power  $\dot{Q}$ , the counterflow velocity  $v_{ns}$  or the normal component Reynolds number  $Re_n$ . All of these dependencies exhibit a slowly growing region, which is not in agreement with the theoretical relation  $L \propto v_{ns}^2$  following from the Vinen equation. Moreover, we measured temporal decay of the quantum turbulence in the same flow and demonstrated scaling with time as  $L \propto 1/t$ . This is in good agreement with the Vinen equation. Additionally, the temperature profile caused by the counterflow was measured and calculated. We observed that the temperature difference drops with the radius as  $1/r^p$ , where  $p$  is between 5 and 6.

Keywords: superfluid helium, quantum turbulence, thermal counterflow, spherical symmetry



# Contents

<b>Introduction</b>	<b>3</b>
<b>1 Theory</b>	<b>7</b>
1.1 Classical Newtonian fluid . . . . .	7
1.1.1 Continuum approach . . . . .	7
1.1.2 Continuity equation . . . . .	7
1.1.3 Momentum equation . . . . .	7
1.1.4 Principle of dynamical similarity . . . . .	8
1.1.5 Classical turbulence . . . . .	9
1.2 Superfluid $^4\text{He}$ . . . . .	10
1.2.1 Superfluidity . . . . .	11
1.2.2 Quantized vortices . . . . .	11
1.2.3 Counterflow turbulence . . . . .	13
1.2.4 Vortex filament model . . . . .	14
1.2.5 HVBK equations . . . . .	15
1.2.6 Temperature profile . . . . .	16
1.2.7 Second sound attenuation . . . . .	17
1.3 Second sound resonances in a spherical cavity . . . . .	18
1.3.1 Approximate analytical solution . . . . .	18
1.3.2 Numerical solution incorporating SS-attenuation . . . . .	19
1.4 VLD profile . . . . .	21
<b>2 Experimental apparatus and control</b>	<b>23</b>
2.1 Cryostat and cooling . . . . .	23
2.2 Temperature control . . . . .	24
2.3 Second sound sensors . . . . .	24
2.4 Spherical resonator . . . . .	25
<b>3 Results</b>	<b>27</b>
3.1 Spherical resonances of second sound . . . . .	27
3.2 Cell overheating . . . . .	31
3.3 Temperature profile measurements . . . . .	33
3.4 Steady state turbulence . . . . .	35
3.5 Decay of turbulence . . . . .	40
<b>4 Discussion</b>	<b>45</b>
4.1 VLD and resonance curve profile . . . . .	45
4.2 Quantum and classical turbulence interplay . . . . .	45
4.3 Local decay . . . . .	47
4.4 Comparison to the thermal counterflow in channel . . . . .	49
<b>Conclusion</b>	<b>51</b>
<b>Bibliography</b>	<b>53</b>

<b>A Attachments</b>	<b>55</b>
A.1 Attachment 1. Spherical Thermal Counterflow of He II . . . . .	55

# Introduction

Probably everyone experiences turbulence during their life, whether it is on a plane or by observing water disappearing into a canal. From the physical point of view, turbulence is usually perceived as chaotic motion of a fluid or, more explicitly, as random fluctuations of the flow velocity. Turbulence can also be characterized by the creation of circulating structures called vortices, which are difficult to describe quantitatively. The influence of turbulence on our lives led to the development of many experimental methods as well as theoretical approaches.

The above mentioned classical-like type of turbulence occurs in all known fluids in Nature. However, in fluids governed by the laws of quantum mechanics such as superfluid helium a similar type of motion exists, usually called *Quantum Turbulence*.

Helium has two stable isotopes  $^3\text{He}$  and  $^4\text{He}$  and in the following text we will consider exclusively the more common and accessible  $^4\text{He}$ . Under normal conditions (room temperature, atmospheric pressure) helium behaves as an inert gas, but condenses into liquid state at 4.2 K. Temperature of the liquid can be lowered further by pumping the saturated vapour. Upon reaching 2.17 K (38 Torr), helium undergoes a second order phase transition, characterized by the discontinuity in its specific heat in the shape of the letter  $\lambda$ . This is the transition to the superfluid state and is called the  $\lambda$ -point. Below 2.17 K, helium is superfluid and is denoted **He II**, possesses unusual properties like very low (or in 0 K limit zero) viscosity, extremely high thermal conductivity and high zero point energy due to low mass and filled s-orbitals. This prevents He II from freezing unless sufficiently high pressure ( $\approx 25$  bar) is applied. The classical liquid helium above 2.17 K is then referred to as **He I**, see Figure 1.

Helium atoms have zero spin, and thus behave as bosonic particles obeying Bose-Einstein distribution and can undergo the Bose-Einstein condensation (first proposed by London [1]). For a non-interacting gas, this would happen at  $T_B \approx 3.15$  K, remarkably close to the observed transition. Above  $T_B$  almost no particles are in the energetic ground state, while below  $T_B$  the number of such particles begins to grow quickly. At low temperature, the De Broglie wavelength exceeds inter-atomic distances which leads to the collective behaviour of the system, thus to superfluidity.

In parallel with London, Tisza came with his two-fluid model [2], in which he considers He II as a fluid with two co-existing components: *normal*, which is viscous and carries the whole entropy of the system, and *superfluid*, inviscid and with zero entropy. It seems to be straightforward to identify the superfluid component with the particles in the condensate and the particles above condensate as the normal component, but this approach does not provide a complete description of superfluidity of He II. A quantitative phenomenological treatment of superfluidity was first suggested by Landau [3], who considered the normal component as an ideal gas of thermal excitations: *phonons* perceived as longitudinal sound waves and *rotons* (in fact phonons with longer wavelength). The dispersion curve  $\varepsilon = f(p)$ , also introduced by Landau and experimentally observed later, has a special shape (see Figure 2) with the roton minimum and it is the presence of this minimum that is important for the existence of superfluidity. We will discuss

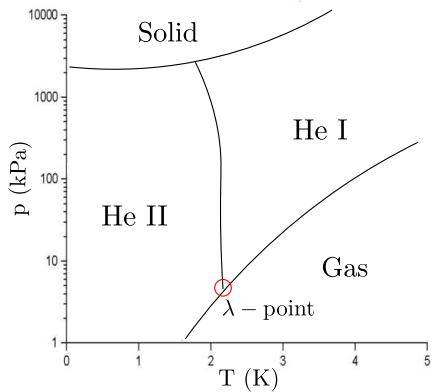


Figure 1: Phase diagram of  $^4\text{He}$ .

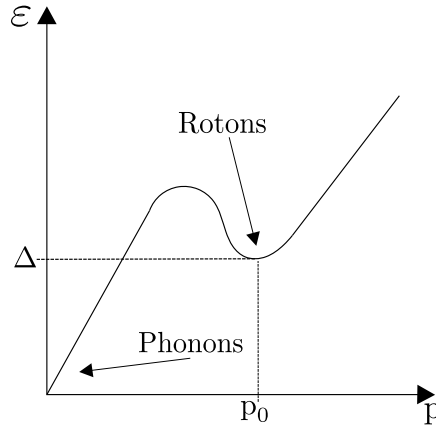


Figure 2: Dispersion relation of thermal excitations in He II.

the theoretical description of He II later in Section 1.2.

As we mentioned above, a special case of turbulent flow can occur in He II, characterized by so-called *Quantized Vortices* present in the inviscid superfluid component. These are essentially topological defects in the superfluid, with fluid circulation quantized in natural multiples of the quantum of circulation  $\kappa$ , described in more detail in Section 1.2.2. These well-defined structures were predicted by Feynmann [4] and indirectly experimentally observed by Yarmchuk and Packard [5] and later directly visualized by Bewley [6] (see Figure 3), providing an interesting object of study on both microscopic and macroscopic scales [7].

Our work follows the previous measurements of quantum turbulence in channels with square cross section, see e.g. Ref. [8], where turbulence was generated by a special flow called *Counterflow* – oppositely flowing normal and superfluid components. Quantized vortices were detected by the attenuation of second sound resonances – oscillations of normal and superfluid components in anti-phase, i.e., standing waves of entropy/temperature. Our goal is to perform similar measurements in spherical geometry, represented by a spherical cell around a point-like heater used for driving the counterflow. This new approach promises to contribute to our understanding of the physical nature of quantum turbulence, and turbulence in general, with emphasis on unbounded flow. Spherically symmetric flow can be investigated in superfluid helium with an advantage, since this symmetry is inaccessible in classical fluids, with the closest analogy found in combustion flows, or diverging jets. The interpretation of our results is based on numerical simulations made by Inui and Tsubota [9], Varga [10] or in the case of cylindrical symmetry, by the Newcastle group [11, 12]. Dedicated simulations of spherically symmetric counterflow were also performed by Róbert Jurčo within his Bachelor Thesis (to be submitted this year), which are also used for comparison.

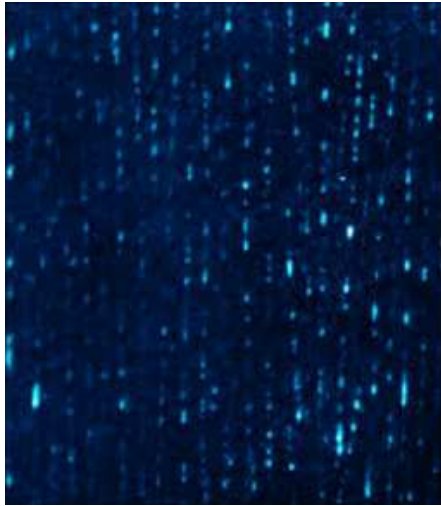


Figure 3: Visualization of quantized vortices in a rotating cryostat using trapped microparticles. Taken from Ref. [6].



# 1. Theory

## 1.1 Classical Newtonian fluid

### 1.1.1 Continuum approach

In the further text we will treat the fluid as a continuum that means time and length scales of intermolecular collisions are much shorter in comparison with the scales of the flow. Specifically, this requires that the Knudsen number  $\text{Kn} = \lambda/l \ll 1$ , where  $\lambda$  is the mean free path of molecules and  $l$  is the smallest relevant length scale of a fluid. Similarly, the Weissenberg number  $\text{Wi} = \omega\tau \ll 1$ , where  $\omega$  is a characteristic frequency of the flow and  $\tau$  is the relaxation time of the fluid. In this case we can suppose the fluid particle contains a sufficiently high number of molecules so that their behaviour can be averaged out [13, 14]. Under these assumptions we will describe a fluid by the Eulerian perspective, when the fluid particle velocity  $\mathbf{v}$ , the density  $\rho$  and also the pressure  $p$  are investigated at a given time  $t$  and position  $\mathbf{r}$  with the respect to an inertial frame of reference.

### 1.1.2 Continuity equation

The local conservation of mass is expressed by the *equation of continuity* (also called as the advection equation):

$$\frac{\partial \rho}{\partial t} + \nabla \cdot (\rho \mathbf{v}) = 0, \quad (1.1)$$

where the first term denotes the time change of the density at a given point and the second term denotes the divergence of the mass flux  $\rho \mathbf{v}$ . In the case of an incompressible fluid, when the density remains constant, equation (1.1) is simplified in the form:

$$\nabla \cdot \mathbf{v} = 0. \quad (1.2)$$

### 1.1.3 Momentum equation

The motion of a fluid is given by the momentum equation, which can be in the general case written as:

$$\frac{\partial(\rho \mathbf{v})}{\partial t} = -\nabla \cdot \mathbf{\Pi}, \quad (1.3)$$

where the momentum flux tensor is given by  $\mathbf{\Pi} = p\mathbf{I} + \rho \mathbf{v} \mathbf{v} - \boldsymbol{\tau}'$ <sup>1</sup>, where  $\boldsymbol{\tau}'$  is the viscous stress tensor causing the transport of momentum due to the viscous friction [14]. Hereafter, we will restrict ourselves to the treatment of Newtonian fluids possessing similar properties as water or liquid helium. This leads to the assumption that the viscous stress tensor is a linear function of the strain tensor and for incompressible fluids we can write:

$$\boldsymbol{\tau}' = \eta \left( \nabla \mathbf{v} + (\nabla \mathbf{v})^\top \right), \quad (1.4)$$

---

<sup>1</sup>The term  $\mathbf{v} \mathbf{v}$  denotes a symmetric tensor of the second order, in components  $\mathbf{v} \mathbf{v} \equiv v_i v_j$ .

where  $\eta$  is the dynamic viscosity and  $\nabla\mathbf{v}$  is the velocity field gradient<sup>2</sup>. Substituting (1.4) into (1.3) considering constant viscosity we get the important *Navier-Stokes equations* (NS-equations) in the incompressible form:

$$\rho\frac{\partial\mathbf{v}}{\partial t} + \underbrace{\rho(\mathbf{v}\cdot\nabla)\mathbf{v}}_{\text{Convective term}} = -\nabla p + \underbrace{\eta\Delta\mathbf{v}}_{\text{Diffusive term}} + \mathbf{f}. \quad (1.5)$$

The nonlinear convective term is unique for fluid mechanics, describing inertial forces acting on continuum particles, while the diffusive term represents the molecular diffusion and collisions and acts to unify the velocity field (viscosity plays similar role here as thermal diffusivity in the heat equation). The first term on the right hand side stands for pressure as a driving force for the fluid, and  $\mathbf{f}$  is an added external volumetric force, for example gravity.

Applying the divergence on the Navier-Stokes equations we can obtain a relation for the pressure called *Poisson equation*, which has the form:

$$\Delta p = -\rho(\nabla\mathbf{v}) : (\nabla\mathbf{v})^\top. \quad (1.6)$$

These three relations (1.2),(1.5),(1.6) obtained above together with the equation of state and the boundary conditions provide a complete set describing incompressible Newtonian fluids [14]. The equation of state is medium dependent. While gases can be described by the ideal gas law, or by van der Waals equation, various empirical models exist for realistic description of liquids, too numerous to mention here. The usual chosen boundary condition is so-called no-slip, which requires the velocity  $\mathbf{v}$  to be zero with respect to the velocity  $\mathbf{V}$  of the boundary (moving body)

$$\mathbf{v} - \mathbf{V} = 0. \quad (1.7)$$

### 1.1.4 Principle of dynamical similarity

Let us consider two independent flow systems with geometrically similar boundaries treated by the NS-equations (1.5) with respect to their inertial frames of reference [13]. We can assign to each of the systems a characteristic length  $L$ , given by the dimensions, and velocity  $U$ , which can be perceived as mean flow velocity. Assuming there is no other characteristic time scale of the flow (such as, e.g., a period of oscillation), one may define dimensionless variables:

$$\hat{\mathbf{r}} = \frac{\mathbf{r}}{L}, \quad \hat{t} = \frac{tU}{L}, \quad \hat{\mathbf{v}} = \frac{\mathbf{v}}{U}, \quad \hat{p} = \frac{p}{\rho U^2}. \quad (1.8)$$

Substituting these new variables into (1.5) we obtain the Navier-Stokes equations in dimensionless form.

$$\frac{\partial\hat{\mathbf{v}}}{\partial\hat{t}} + (\hat{\mathbf{v}}\cdot\hat{\nabla})\hat{\mathbf{v}} = -\hat{\nabla}\hat{p} + \frac{1}{\text{Re}}\hat{\Delta}\hat{\mathbf{v}} \quad (1.9)$$

$$\text{Re} = \frac{UL}{\nu} \quad (1.10)$$

---

<sup>2</sup> $\nabla\mathbf{v} \equiv \partial v_i/\partial x_j$

Only one relevant parameter  $Re$  describing these two flows remains, called the *Reynolds number*. Flows with similar  $Re$  then can be considered as dynamically similar, meaning they are governed by the same dynamical equation. The Reynolds number also conveniently describes the ratio between the nonlinear and viscous forces, and therefore is very often used to determine if a flow is laminar or turbulent.

### 1.1.5 Classical turbulence

Turbulence itself is still not a completely solved and understood problem. It is usual to imagine turbulence as a chaotic disordered flow characterized by non-negligible fluctuations of velocity arising due to the convective term in (1.5). As written above, the Reynolds number is a parameter determining if the flow is turbulent, or not. In the case of high  $Re$  the viscous dissipative term is negligible and the dominant non-linear term tends to produce perturbations in the velocity. For low  $Re$  is the situation opposite, the viscous term wins and the flow is laminar.

For these reasons, turbulence must be described in a statistical sense, i.e., using mean values and their fluctuations. Considering that, the Reynolds decomposition of the velocity field [13] is introduced:

$$\mathbf{v} = \langle \mathbf{v} \rangle + \mathbf{v}', \quad (1.11)$$

when the velocity is decomposed into its temporal mean value  $\langle \mathbf{v} \rangle$  and a random fluctuation  $\mathbf{v}'$ , which satisfies  $\langle \mathbf{v}' \rangle = 0$ . The same process can be repeated for pressure. Substituting the decomposed velocity into (1.5) and averaging the whole equation with respect to time, we get *Reynolds-averaged Navier-Stokes equations* (RANS)[13]:

$$\rho \frac{\partial \langle \mathbf{v} \rangle}{\partial t} + \rho (\langle \mathbf{v} \rangle \cdot \nabla) \langle \mathbf{v} \rangle = -\nabla \langle p \rangle + \eta \Delta \langle \mathbf{v} \rangle - \rho \nabla \cdot \underbrace{\langle \mathbf{v}' \mathbf{v}' \rangle}_{\text{Reynolds stress}}. \quad (1.12)$$

A new term, originating from the convective term, appears on the right-hand side. This Reynolds stress tensor expresses the momentum transfer due to the turbulent motion of the fluid and has an effect on  $\langle \mathbf{v} \rangle$ . It is necessary to emphasize that the system of RANS, the Poisson equation and the equation of state, is not closed, and the Reynolds stress must be given in some other way. Despite that, the RANS are very often used for numerical simulation of turbulent flows, because the approach of Reynolds decomposition carries less computational costs than direct numerical simulations of NS-equations. It is possible to impose the so-called eddy viscosity and make the equations even simpler, but that is beyond the scope of this Thesis. In general, the RANS are very good for computing and modelling turbulence in the continuum approach but do not say much about its qualitative properties and its structure.

Turbulence always contains rotary motion and can be thought of as consisting of individual vortices, or eddies. The velocity circulation around the core of the eddy is described by its vorticity defined as  $\boldsymbol{\omega} = \nabla \times \mathbf{v}$ . It is also possible to derive equations for  $\boldsymbol{\omega}$  by taking a curl of (1.5). Turbulent flows usually contain such vortices of different characteristic dimensions, often spanning several decades of length scales. These vortices undergo the so-called *Richardson cascade*,

when the largest vortices gradually decay into smaller ones until at some point, viscous dissipation will convert their energy to heat. Turbulence is assumed to be homogeneous and isotropic at these small length scales, dominated by viscous dissipation. On the other hand, at length scales much higher than this dissipation length scale, the role of viscosity can be entirely neglected. The turbulent flow consists of large energetic vortices, of typical dimension  $L$ , called the integral length scale. Turbulence composed of such vortices is very non-homogeneous and anisotropic, since boundaries of the domain affect them. The problem of viscous dissipation and energy transfer in the vortex cascade is the essence of the Kolmogorov theory [15]. The only relevant parameters of the theory are kinematic viscosity  $\nu = \eta/\rho$  and the dissipation rate  $\varepsilon$ . Taking into account these variables, it is possible to define from dimensional analysis the so-called *Kolmogorov microscale*:

$$\lambda_0 = \left( \frac{\nu^3}{\varepsilon} \right)^{1/4}. \quad (1.13)$$

This scale is characteristic of the smallest vortices which dissipate energy and corresponds to  $\text{Re} \approx 1$ .

Other Kolmogorov assumptions concern length scales between  $L$  and  $\lambda_0$  far from both. In this *inertial subrange*, energy is transferred from the large vortices to the small, and it is described by only one parameter – the energy transfer rate  $\varepsilon$ , which is equal to the dissipation rate. Considering this, we can derive the well known Kolmogorov spectrum for the inertial subrange:

$$E(k) = C\varepsilon^{2/3}k^{-5/3}, \quad (1.14)$$

where  $k$  is the wavenumber, a reciprocal quantity to the length scale. The experimentally determined constant  $C$  is approximately equal to 1.5.

We can divide the length scales represented in the flow into three ranges: energy containing range, corresponding to the largest vortices, the inertial subrange and the dissipation range, as one may see in Figure 1.1.

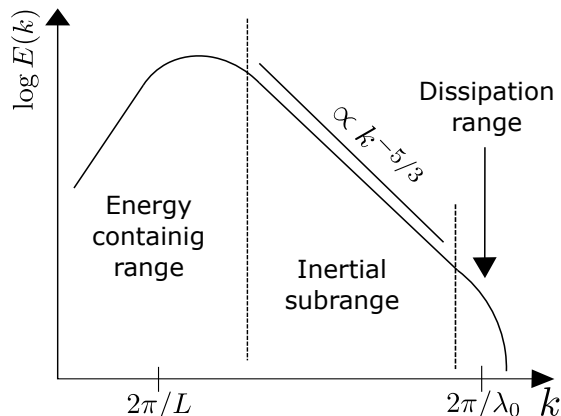


Figure 1.1: Kolmogorov energy spectrum in logarithmic scales.

## 1.2 Superfluid $^4\text{He}$

As mentioned in the Introduction, the superfluid  $^4\text{He}$  or just He II is considered as a two-component fluid with the inviscid superfluid and the classical-like viscous

component. Each of the components can be matched with its own velocity  $\mathbf{v}_s, \mathbf{v}_n$  and density  $\rho_s, \rho_n$ . The densities are temperature-dependent, and around 1.0 K He II is almost completely superfluid. He II also possesses interesting unusual properties, which cannot be completely understood by the classical continuum approach.

### 1.2.1 Superfluidity

The main peculiarity is the ability of fluid to flow without any viscous friction. As we will show, superfluidity is a consequence of an interaction between helium atoms. Considering this, Landau looked at He II as a gas of thermal excitations, phonons and rotons, with unique dispersion relation, see Figure 2. The linear part can be described similarly as longwave phonons (elastic vibrations, sound waves) in crystalline matter:

$$\varepsilon = C_1 p, \quad (1.15)$$

where  $C_1$  is the speed of sound [16]. In the case of a fluid, we consider only longitudinal phonons due to negligible shear stresses. The nonlinear part belonging to rotons is usually considered quadratic:

$$\varepsilon = \Delta + \frac{(p - p_0)^2}{2\mu}, \quad (1.16)$$

where  $\Delta$  is the energy gap,  $p_0$  the momentum corresponding to the roton minimum and  $\mu$  is the roton effective mass.

Now we will clarify the problem of superfluidity of He II. Let us consider a particle moving through the static superfluid component with velocity  $\mathbf{V}$  and mass  $M$ . This particle will produce an excitation with energy  $\varepsilon(p)$  due to interactions with condensate atoms. Then equations of the conservation of momentum and energy must hold. From these equations, it is possible to derive the Landau criterion of superfluidity with the critical velocity  $v_L$  given by:

$$v_L = \min \left( \frac{\varepsilon(p)}{p} \right), \quad (1.17)$$

where  $p$  is the momentum of the excitation. For phonons  $v_L \approx 239$  m/s and for rotons  $v_L \approx 58$  m/s [17]. It means superfluidity can occur at non-zero velocity, even though interactions are, in principle, present. Conversely, the parabolic dispersion relation for free particles  $\varepsilon = p^2/(2m)$ , would give  $v_L \approx 0$  m/s, i.e., the presence of interactions between helium atoms is essential for superfluidity.

### 1.2.2 Quantized vortices

Quantized vortices follow from the quantum nature of the superfluid component, which is considered a Bose-Einstein condensate. A collective behaviour of He atoms under sufficiently low temperature, in the case of  $^4\text{He}$  under 2.17 K, leads us to describe this system by a macroscopic wave function  $\Psi(\mathbf{r}, t)$ , which is related to the superfluid density by the well-known quantum-mechanical formula  $\rho_s(\mathbf{r}, t) = |\Psi(\mathbf{r}, t)|^2$ . It is necessary to point out that we approximate the many-particle problem, with a ground-state one-particle wave function holding for every particle

in the condensate [18]. The wavefunction  $\Psi(\mathbf{r}, t)$  can be generally obtained as a solution of the Schrödinger equation containing an interacting non-linear term, for weakly interacting gas, called the Gross-Pitaevskii equation (GPE). The solution is usually considered in the form:

$$\Psi(\mathbf{r}, t) = \sqrt{\rho_s(\mathbf{r}, t)} e^{i\phi(\mathbf{r}, t)}, \quad (1.18)$$

where  $\phi(\mathbf{r}, t)$  is a macroscopic phase. Now we should remember the relation for quantum probability flux:

$$\mathbf{j} = -\frac{\hbar i}{2m_4} [\Psi^*(\nabla\Psi) - \Psi(\nabla\Psi^*)]. \quad (1.19)$$

Substituting (1.18) to (1.19) and using  $\mathbf{j} = \rho_s \mathbf{v}_s$ , we arrive at:

$$\mathbf{v}_s(\mathbf{r}, t) = \frac{\hbar}{m_4} \nabla\phi(\mathbf{r}, t). \quad (1.20)$$

From (1.20) we see that the gradient of the macroscopic phase gives the superfluid velocity, i.e., the flow of the superfluid component is potential. The potential flow is also irrotational  $\nabla \times \mathbf{v}_s = 0$ , which indicates no classical-like turbulence should be possible in the superfluid component. To be accurate, one situation with non-zero circulation exists. Let us consider circulating  $\mathbf{v}_s$  along a closed curve  $\gamma$ :

$$\Gamma = \oint_{\gamma} \mathbf{v}_s \cdot d\mathbf{l} = \frac{\hbar}{m_4} \oint_{\gamma} \nabla\phi(\mathbf{r}, t) \cdot d\mathbf{l}. \quad (1.21)$$

To obtain  $\Gamma \neq 0$ , the region with the trajectory  $\gamma$  must be multiply connected, i.e., a hole must appear somewhere in the closed  $\gamma$ -loop. Due to the fact that the wave function can not change after one round along  $\gamma$ , the only possible change of  $\phi$  is in multiples of  $2\pi$ . Following that, the circulation is quantized:

$$\Gamma = \frac{\hbar}{m_4} 2\pi n = \kappa n, \quad (1.22)$$

where  $\kappa = 9.98 \cdot 10^{-8} \text{ m}^2/\text{s}$  is the *Quantum of circulation*. This means that the superfluid component can create holes in itself and circulate around them, and this is consistent with experimental observation of a meniscus forming on the level of He II. These “holes” are called *Quantized vortices*, introduced as topological defects or, simply, as thin lines with approximately  $1\text{\AA}$  core. They must form closed loops – vortex rings, or begin and finish on a boundary due to the conservation of circulation (Kelvin’s theorem).

It can be shown from GPE that superfluidity is suppressed in the vortex core, and  $\mathbf{v}_s$  falls with the radius from the middle of the vortex as  $1/r$ . Most of the vortices are only once quantized, as it is energetically favourable. Their nucleation in He II can be caused by exceeding a certain critical velocity, from seed loops pinned at walls that were created in previous experiments, or during the crossing of the lambda transition via the Kibble-Zurek mechanism. It was observed that the level of rotating He II indeed has the same meniscus as it is in classical fluids, and that a regular grid of quantized vortices with the density  $n = 2\Omega/\kappa$  is created.

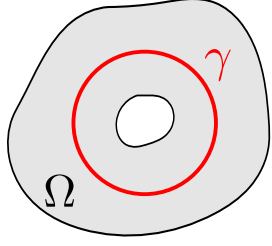


Figure 1.2: Example of a multiply connected region  $\Omega$ .

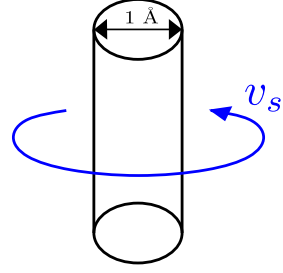


Figure 1.3: Sketch of a quantized vortex.

The decay of quantized vortices can be caused by interaction with vortices of opposite circulation, by shrinking when emitting phonons due to the presence of Kelvin's waves – vibrations of the vortex line, or by interaction with the normal component. Indeed, the occurrence of quantized vortices in He II is substantial for coupling of the normal and the superfluid component, which is described by the Mutual friction force (1.35).

Dynamical interactions between quantized vortices lead us to the concept of *Quantum turbulence*. We are interested in quantum turbulence generated via a particular type of flow – thermal counterflow.

### 1.2.3 Counterflow turbulence

Counterflow, or better, thermal counterflow is a type of flow when the normal and the superfluid component stream against each other with zero mass transfer. So it is convenient to define the *counterflow velocity*:

$$\mathbf{v}_{ns} = \mathbf{v}_n - \mathbf{v}_s, \quad (1.23)$$

an important quantitative parameter for the characterization of our flow. Counterflow can be easily driven by applying heat into the helium bath. The superfluid component will be transformed to the normal in the vicinity of the heater. The normal component will flow away and will be replaced by a new amount of superfluid, since the equation of continuity must hold. Considering the following set of equations, respectively, the conservation of entropy, the equation of continuity for incompressible He II, and the sum of densities:

$$\frac{\dot{Q}}{T} = \rho_s A v_n, \quad \rho_s \mathbf{v}_s + \rho_n \mathbf{v}_n = 0, \quad \rho = \rho_s + \rho_n \quad (1.24)$$

it is possible, together with (1.23), to derive a relation for the magnitude of  $\mathbf{v}_{ns}$ :

$$v_{ns} = \frac{\dot{Q}}{\rho_s s T A}. \quad (1.25)$$

Here,  $A$  is an area with a normal parallel to the direction of the heat flux  $\rho_s T \mathbf{v}_n$ , with  $s$  the entropy per unit mass and  $\dot{Q}$  is the power applied to the heater.

Thermal counterflow can generate turbulence in both components, in the normal component characterized by perturbation in velocity and in the superfluid by quantized vortices. We are seeking the amount of vortices created due to the

counterflow. The indirectly measurable quantity providing a mean distribution of vortices in the system, is called *vortex line density* (VLD), denoted by  $L$  – total length of vortices per unit volume. The equation describing the time evolution of  $L$  in the  $\mathbf{v}_{ns}$ -field was derived by Vinen [19]:

$$\frac{dL}{dt} = \left(\frac{dL}{dt}\right)_{gen} + \left(\frac{dL}{dt}\right)_{decay} = av_{ns}L^{3/2} + g(v_{ns}) - bL^2, \quad (1.26)$$

$$a = \alpha\chi_1, \quad b = \frac{\kappa}{2\pi}\chi_2, \quad (1.27)$$

where  $\chi_1, \chi_2$  are factors of order unity and  $\alpha$  is the temperature dependent mutual friction coefficient. The first generating term is based on the force acting on expanding vortex rings together with dimensional analysis. The unknown function  $g(v_{ns})$  is added to cover the emergence of vortices, which is not included in the generating term and usually is neglected in calculations. The second decaying term assumes annihilation of oppositely oriented vortices in the homogeneous vortex tangle.

We can derive two unique solutions of this Vinen equation. The first holds for the steady-state turbulence when the overall time derivative of  $L$  equals zero. Then we have for  $L$  the formula:

$$L \approx \gamma^2 v_{ns}^2, \quad (1.28)$$

where the coefficient  $\gamma$  is usually determined by experimental observations. The second is the equation for temporal decay of the vortex tangle when we assume the generating term is zero.

$$L \approx \frac{L_i}{t + t_0} + L_0, \quad (1.29)$$

where  $L_i$  and  $L_0$  are, respectively, the constant factor of the decaying law and the final remaining VLD, representing vortices that are impossible to remove from the bath (without increasing the temperature) since they are attached to solid bodies.

## 1.2.4 Vortex filament model

This mesoscopic approach to quantum turbulence is very useful to simulate a motion of a large bundle of vortices numerically. The vortex is considered as a thin, one-dimensional line in space mathematically described as a parametric curve  $\mathbf{s} = \mathbf{s}(\xi, t)$ , where  $\xi$  is the arclength. Two forces act on the vortex, Magnus force perpendicular to the tangent  $\mathbf{s}' = d\mathbf{s}/d\xi$  as a consequence of circulation causing pressure differences in the flowing fluid, and drag force caused by scattering of the normal component on the vortex. In the stationary state, these forces must be equal and we obtain the so-called *Schwarz equation* [20]:

$$\mathbf{v}_L = \frac{d\mathbf{s}}{dt} = \mathbf{v}_s + \mathbf{v}_i + \alpha\mathbf{s}' \times (\mathbf{v}_{ns} - \mathbf{v}_i) - \alpha'\mathbf{s}' \times [\mathbf{s}' \times (\mathbf{v}_{ns} - \mathbf{v}_i)], \quad (1.30)$$

where  $\alpha'$  is the second mutual friction coefficient, and  $\mathbf{v}_i$  is the velocity induced by the vortex itself and by other nearby vortices, and is given by the Biot-Savart law:

$$\mathbf{v}_i(\mathbf{r}) = \frac{\kappa}{4\pi} \int \frac{d\mathbf{s} \times (\mathbf{r} - \mathbf{s})}{|\mathbf{r} - \mathbf{s}|^3}. \quad (1.31)$$

The integration should be made along the whole vortex line and can be split into two parts – local (due to the local curvature of the vortex itself) and non-local (effects of all other vortices). Since we consider the vortex line as a one-dimensional object, the local part has a singularity and usually is approximated by the following relation:

$$\mathbf{v}_{SI} \approx \beta(\mathbf{s}' \times \mathbf{s}''), \quad (1.32)$$

$$\beta = \frac{\kappa}{4\pi} \ln\left(\frac{R}{a}\right), \quad (1.33)$$

where  $R$ , and  $a$ , are, respectively, the radius of curvature, the diameter of the vortex core and  $\mathbf{s}'' = d^2\mathbf{s}/d\xi^2$ .

This approach introduces certain difficulties, as it differs from the real situation in several important aspects. It is impossible to cover the emergence of vortices, thus initial vortices must be imposed, and vortex reconnections and dissipation must be prescribed artificially in some way. A similar problem exists with macroscopic velocity fields  $\mathbf{v}_s$  and  $\mathbf{v}_n$ , i.e.,  $\mathbf{v}_{ns}$ .

### 1.2.5 HVBK equations

We still need a description, how the macroscopic velocity fields  $\mathbf{v}_s$  and  $\mathbf{v}_n$  behave in space and time. In the simplest case, neglecting quantized vortices and the thermo-mechanical effect, it is possible to treat the motion of the normal component by the NS-equations (1.5) and the superfluid by the Euler equations, since its viscosity is zero. The thermo-mechanical effect (force  $\rho_s s \nabla T$ ) is another consequence of the two-fluid behaviour when a temperature gradient causes a gradient of pressure [14].

The biggest problem is hidden in the introduction of quantized vortices in the continuum approach, since the presence of a chaotic discreet vortex bundle highly disturbs our idea of the continuum particle. The proposed solution assumes that vortices are parallel aligned in the continuum particle and a macroscopic vorticity  $\boldsymbol{\omega}_s$  is introduced as a mean vorticity around every vortex in the studied particle.

The two above-mentioned effects and the assumption of the macroscopic vorticity are included in the *Hall–Vinen–Bekarevich–Khalatnikov (HVBK) equations*.

$$\begin{aligned} \rho_n \left( \frac{\partial \mathbf{v}_n}{\partial t} + (\mathbf{v}_n \cdot \nabla) \mathbf{v}_n \right) &= -\frac{\rho_n}{\rho} \nabla p - \rho_s s \nabla T + \eta \Delta \mathbf{v}_n + \frac{\rho_n \rho_s}{\rho} \mathbf{F}_{ns}, \\ \rho_s \left( \frac{\partial \mathbf{v}_s}{\partial t} + (\mathbf{v}_s \cdot \nabla) \mathbf{v}_s \right) &= -\frac{\rho_s}{\rho} \nabla p + \rho_s s \nabla T + \mathbf{T} - \frac{\rho_n \rho_s}{\rho} \mathbf{F}_{ns}. \end{aligned} \quad (1.34)$$

Here,  $\mathbf{T}$  is the vortex tension force (analogy to a tension of a classical string), and this term is usually omitted as its influence on the macroscopic field is not significant. The mutual friction force  $\mathbf{F}_{ns}$  is coupling the components together and has the same origin as the drag force acting on quantized vortices mentioned above. It is given by:

$$\mathbf{F}_{ns} = \frac{B}{2} \hat{\boldsymbol{\omega}}_s \times (\boldsymbol{\omega}_s \times \mathbf{v}_{ns}) + \frac{B'}{2} \boldsymbol{\omega}_s \times \mathbf{v}_{ns}, \quad (1.35)$$

where  $B, B'$  are density-independent mutual friction coefficients related to  $\alpha, \alpha'$  as  $\alpha = (\rho_n B)/(2\rho), \alpha' = (\rho_n B')/(2\rho)$ . The unit vector  $\hat{\boldsymbol{\omega}}_s$  has the direction of  $\boldsymbol{\omega}_s$ .

In the frame of the HVBK-approach, it is possible to write an approximative relation for vortex line density:

$$L = \frac{\omega_s}{\kappa}. \quad (1.36)$$

We can substitute this into (1.35), assume for simplicity the perpendicularity of  $\mathbf{v}_{ns}$  to  $\boldsymbol{\omega}_s$  (as vortices tend to orient perpendicularly to counterflow) and omit the conservative term with  $B'$  perpendicular to  $\mathbf{v}_{ns}$ , then a simplified form of (1.35) is derived

$$\mathbf{F}_{ns} = -\frac{B}{2}\kappa L\mathbf{v}_{ns}. \quad (1.37)$$

## 1.2.6 Temperature profile

As we indicated above, counterflow is accompanied by an emergence of a temperature profile, i.e, a gradient of temperature. The presence of the temperature profile is essential for the steady state solution of HVBK-equations (1.34) as it was calculated in cylindrical geometry [11]. Taking into account the geometry of the experimental cell described in the section 2.4, we can consider the flow as spherically symmetric. Only the radial component of  $\mathbf{v}_{ns}$  is relevant and HVBK-equations(1.34), in the stationary case, can be rewritten as:

$$\begin{aligned} \rho_n v_n \frac{\partial v_n}{\partial r} &= -\frac{\rho_n}{\rho} \frac{\partial p}{\partial r} - \rho_s s \frac{\partial T}{\partial r} + \eta \Delta_r v_n + \frac{\rho_n \rho_s}{\rho} \mathbf{F}_{ns} \cdot \hat{\mathbf{r}}, \\ \rho_s v_s \frac{\partial v_s}{\partial r} &= -\frac{\rho_s}{\rho} \frac{\partial p}{\partial r} + \rho_s s \frac{\partial T}{\partial r} - \frac{\rho_n \rho_s}{\rho} \mathbf{F}_{ns} \cdot \hat{\mathbf{r}}. \end{aligned} \quad (1.38)$$

Here,  $\Delta_r$  is the radial part of the Laplace operator<sup>3</sup>. Now we can obtain  $\partial T/\partial r$ , taking into account fundamental relations holding for the two-fluid model (1.23), (1.24) together with the simplified form of the mutual friction force (1.37).

$$\rho_s \frac{\partial T}{\partial r} = -\frac{\rho_n}{2} \frac{\partial}{\partial r} \left[ v_n^2 \left( 1 - \frac{\rho_n^2}{\rho_s^2} \right) \right] + \eta \Delta_r v_n - \frac{B\kappa}{2} \frac{\rho_n \rho}{\rho_s} L v_n. \quad (1.39)$$

For this spherical case, the normal fluid velocity can be calculated as  $v_n = \dot{Q}/(4\pi\rho_s T r^2)$ . Determination of a correct VLD-profile  $L(r)$  is still under the scope of experimental and theoretical research, therefore we will take the formula following from the Vinen equation (1.26)  $L \approx \gamma^2 v_{ns}^2 = (\gamma \rho v_n)^2 / \rho_s^2$ .

The temperature profile given by (1.39) has to be calculated numerically using a simple 1D finite differences approach. The result is compared with experimental observations in Chapter 3.3.

We can also provide an approximative solution. It is possible to show that the classical viscous term is negligible compared to the other two terms on the right-hand side. The first term is proportional to the distance as  $1/r^5$  and the third term as  $1/r^6$ . From the calculation, the term  $1/r^6$  is stronger for a sufficiently high power (around 500 mW at 1.65 K) and distances smaller than 10 mm, which corresponds to the radius of our cell. Neglecting also the first term and assuming temperature variations between the heater and the bath are small, which means

---

<sup>3</sup> $\Delta_r v_n = \frac{1}{r^2} \frac{\partial}{\partial r} \left( r^2 \frac{\partial v_n}{\partial r} \right)$

other variables remain constant, the approximative relation for  $T(r)$  is obtained by integration:

$$T(r) = T_0 + \frac{\alpha\kappa\gamma^2}{5s^4\rho_s^3} \left( \frac{\dot{Q}}{4\pi T_0} \right)^3 \frac{1}{r^5}, \quad (1.40)$$

where  $T_0$  is the bath temperature or better the temperature at infinity. These theoretical results together with experimental data have been already published by our group in Ref. [21], included as an Appendix to this Thesis.

### 1.2.7 Second sound attenuation

Not only classical sound waves, waves of pressure or density, can propagate in He II. The two-fluid behaviour enables the existence of other sound modes [22], the crucial one for our research is the so-called *Second sound* (SS). The total density  $\rho = \rho_n + \rho_s$  remains constant, but the ratio of component densities changes when they oscillate with opposite phases. Since the entropy of the superfluid part is zero, the oscillations are connected with an entropy periodic change, i.e., with temperature waves. We know the presence of quantized vortices couples He II components together, so it must have a non-negligible effect on second sound. Especially, we seek resonances when the attenuating effect due to scattering on vortices is apparent.

Assuming the second sound wave as a plane wave of  $\mathbf{v}_{ns}$  travelling in the  $z$ -direction, it is possible to show, by few steps with (1.34),(1.35), the wave vector in the first order of the Taylor expansion has the form:

$$k = -\frac{\omega}{c_2} \left( 1 - i \frac{B\kappa L}{4\omega} \sin^2(\theta) \right). \quad (1.41)$$

The imaginary part of the wave has the physical meaning of dissipation, which is a linear function of  $L$ . The  $c_2$  is the temperature-dependent second sound velocity, see Figure 1.4. The angle  $\theta$  is the polar angle between  $\mathbf{L}$  and  $\mathbf{v}_{ns}$ , and in the case of homogeneous and isotropic turbulence, we can take the mean value  $\langle \sin^2(\theta) \rangle = 2/3$ . Since the attenuation is considered linear, the measured resonance peak has the Lorentzian shape.

Moreover, we can introduce the relation between the VLD and the damped amplitude  $A$  of the SS resonance [23]:

$$L = \frac{6\pi\Delta f}{B\kappa} \left( \frac{A_0}{A} - 1 \right), \quad (1.42)$$

where  $A_0$  is the amplitude of the SS resonance in the flow without quantized vortices and  $\Delta f$  the width of the unattenuated resonance curve. At the end of this subsection, we should emphasize that the attenuation, the energy dissipated in the system, is inversely proportional to the quality factor of the resonator  $Q = f_0/\Delta f$ .

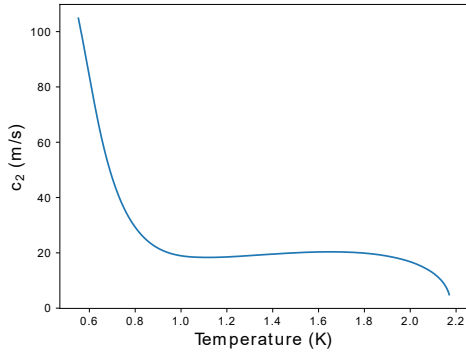


Figure 1.4: The temperature dependence of the second sound speed  $c_2$ . The local maximum lies around 1.65 K. Values are taken from Ref. [16].

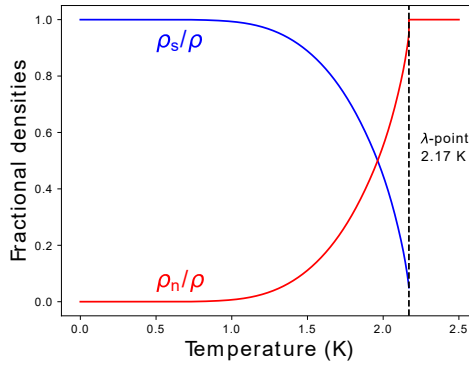


Figure 1.5: The temperature dependence of the normal and superfluid density. Values are taken from Ref. [16].

## 1.3 Second sound resonances in a spherical cavity

### 1.3.1 Approximate analytical solution

We seek frequencies belonging to standing waves in a spherical cavity. This problem is slightly more complicated than in the classical 1D-resonator, since we need to treat it in spherical coordinates  $(x, y, z) \rightarrow (r, \vartheta, \varphi)$ . When we neglect dissipation, it is convenient to assume the counterflow velocity as a gradient of a scalar potential  $\mathbf{v}_{ns} = \nabla\phi$ . The function  $\phi$  can be obtained as a wave equation solution:

$$\nabla\phi - \frac{1}{c_2} \frac{\partial^2\phi}{\partial t^2} = 0. \quad (1.43)$$

To find a general solution of (1.43), we will assume it as a product of two independent parts – spatial and temporal, i.e.,  $\phi(\mathbf{r}, t) = \Phi(\mathbf{r})\Upsilon(t)$ . If we substitute this into (1.43), using the separation constant  $k^2$  we get two independent equations. The solution of the time-dependent equation can be written in the well-known form  $\Upsilon(t) \propto \exp(i\omega t)$ . To obtain the spatial part, we must investigate solutions of the *Helmholtz equation*:

$$\Delta\Phi(\mathbf{r}) + k^2\Phi(\mathbf{r}) = 0. \quad (1.44)$$

From the mathematical point of view, our problem is restricted to the seeking for eigenvalues and eigenfunctions of the Laplace operator. Fortunately the general solution in spherical coordinates is well-known:

$$\Phi(\mathbf{r}) = \sum_{l=0}^{+\infty} \sum_{m=-l}^{+l} (\alpha_{lm}j_l(kr) + \beta_{lm}y_l(kr))Y_l^m(\vartheta, \varphi). \quad (1.45)$$

We see (1.45) has a radial and an angular part. The radial part is given by so-called spherical Bessel  $j_l$  and Neumann  $y_l$  functions, and the angular by spherical harmonics  $Y_l^m$ . Real numbers  $\alpha_{lm}$ ,  $\beta_{lm}$  are determined by boundary conditions. The number  $l$  denotes the order of the spherical Bessel and Neumann functions,

and in the case of spherical harmonics, the number  $m$  runs from  $-l$  to  $l$  with the increment  $+1$ .

In our case, we seek standing waves between two concentric spheres, the inner sphere with radius  $R_1$  represents the surface of the heater and the outer  $R_2$  wall of the spherical cavity. The spherical harmonics do not affect resonance frequencies, therefore we can investigate only the radial part of the solution. Since the velocity at the boundary must be zero, we get:

$$\left. \frac{\partial \Phi}{\partial r} \right|_{r=R_1} = 0 \quad \left. \frac{\partial \Phi}{\partial r} \right|_{r=R_2} = 0. \quad (1.46)$$

Putting together (1.45) and (1.46), we get a set of simple equations:

$$\begin{aligned} \alpha_l j_l'(kR_1) + \beta_l y_l'(kR_1) &= 0, \\ \alpha_l j_l'(kR_2) + \beta_l y_l'(kR_2) &= 0. \end{aligned} \quad (1.47)$$

We can take a determinant of this set to eliminate coefficients and find the zeros  $k_{ln}$  numerically. Resonance frequencies can be then easily calculated as:

$$f_{ln} = \frac{c_2 k_{ln}}{2\pi}, \quad (1.48)$$

where  $k_{ln}$  denotes the  $n$ -th zero of the  $l$ -th radial function.

### 1.3.2 Numerical solution incorporating SS-attenuation

The previous analytic approach has several problems. The first concerning energy dissipation was already mentioned. The second is hidden in the incorrect boundary condition. The SS-wave is in our experiment driven by so-called Second sound sensors, which we can imagine as a capacitor consisting of a permeable membrane stretched over a brass electrode. One sensor works like a transmitter and one as a receiver. We shall see the boundary condition at the sensors is different, since they must not be fully reflective and can possess some non-zero transmittance. This transmittance can effectively change the dimension of the cell.

The equation incorporating attenuation can be obtained from the HVBK equations (1.34), considering the relation for the mutual friction force (1.35) without the conservative term perpendicular to  $\mathbf{v}_{ns}$ . The detailed derivation can be found for example in the article [23], giving:

$$\nabla(\nabla \cdot \mathbf{v}_{ns}) + \frac{\omega^2}{c_2^2} \left( 1 + i \frac{B\kappa L}{2\omega} \sin^2(\theta) \right) \mathbf{v}_{ns} = 0. \quad (1.49)$$

To solve (1.49) analytically with correct boundary conditions, which are similar to the experimental reality, together with the angular dependence, is highly non-trivial. Thus it is a task for a suitable numerical approach.

*Particular acknowledgement to Mgr. Jakub Kvorka from the Department of Geophysics, who suggested, programmed and executed the numerical approach to the solution of (1.49) using the Spectral decomposition method.*

The solution of (1.49) is assumed in the form  $\mathbf{v}_{ns} = v_r(r, \theta)\hat{\mathbf{r}} + v_\theta(r, \theta)\hat{\boldsymbol{\theta}}$ , i.e., we added the angular-dependent part of velocity  $v_\theta(r, \theta)$ , considering only a dependence on the polar angle  $\theta$ . The  $\hat{\mathbf{r}}$  and  $\hat{\boldsymbol{\theta}}$  are unit vectors. SS sensors are placed exactly on the north and on the south pole of the cell at the positions  $\theta \in \langle 0; \theta_d \rangle$  for the transmitter and  $\theta \in \langle \pi - \theta_d; \pi \rangle$  for the receiver, since they are considered to be circular with diameter 7.5 mm, where  $\theta_d \approx 0.375$  rad.

The boundary condition/the radial velocity profile on the emitter is modelled approximately by a cosine function:

$$v_r|_{emitter} = \cos\left(\frac{\pi\theta}{2\theta_d}\right). \quad (1.50)$$

The determination of the boundary condition on the receiver seems to be less trivial, since the membrane will move under the incoming SS wave, but the electrode will immediately reflect the wave back towards the membrane. For these reasons, the simple Dirichlet boundary condition was chosen:

$$v_r|_{receiver} = 0. \quad (1.51)$$

For the rest of the outer and the inner sphere, the radial component of velocity is assumed to be also zero.

For further numerical calculation the solution of (1.49) is decomposed into the set of basis functions:

$$\mathbf{v}_{ns} = \sum_{l=0}^{+\infty} \sum_{m=-l}^{+l} (y_{lm}\mathbf{Y}_{lm} + \psi_{lm}\boldsymbol{\psi}_{lm} + \Phi_{lm}\boldsymbol{\Phi}_{lm}), \quad (1.52)$$

where the basis consists of the vector spherical harmonics:

$$\mathbf{Y}_{lm} = Y_{lm}\hat{\mathbf{r}}, \quad (1.53)$$

$$\boldsymbol{\psi}_{lm} = \frac{1}{\sqrt{l(l+1)}}r\nabla Y_{lm}, \quad (1.54)$$

$$\boldsymbol{\Phi}_{lm} = \frac{1}{\sqrt{l(l+1)}}\mathbf{r} \times \nabla Y_{lm}. \quad (1.55)$$

Since the boundary condition is only radial, the coefficients in front of the last basis function are identically zero and we seek for coefficients  $y_{lm}$ ,  $\psi_{lm}$  only. Substituting these relations in (1.49), we can arrive to the set of equations for  $y_{lm}$  and  $\psi_{lm}$ , which hold for every  $l, m$ :

$$\frac{\partial}{\partial r} \left( \frac{1}{r^2} \frac{\partial}{\partial r} (r^2 y_{lm}) - \frac{\sqrt{l(l+1)}}{r} \psi_{lm} \right) + \sigma(r) y_{lm} = 0, \quad (1.56)$$

$$\frac{\sqrt{l(l+1)}}{r} \left( \frac{1}{r^2} \frac{\partial}{\partial r} (r^2 y_{lm}) - \frac{\sqrt{l(l+1)}}{r} \psi_{lm} \right) + \sigma(r) \psi_{lm} = 0, \quad (1.57)$$

where  $\sigma(r) = (\omega^2 + i\alpha(r)\omega)/c_2^2$  and  $\alpha(r) = (B\kappa L(r))/3$ . The boundary condition is decomposed in a similar way.

The numerics is then performed on a Chebyshev radial grid, which possesses uneven spacing convenient for such simulation. The differential matrix  $A$  is constructed and the whole problem is transformed into a solution of a classical matrix problem  $A\mathbf{x} = \mathbf{b}$ . We seek the vector  $\mathbf{x}$  containing both  $y_{lm}$  and  $\psi_{lm}$  for the given angular frequency  $\omega$  and boundary condition  $\mathbf{b}$ . This algorithm is quite numerical friendly, since the matrix  $A$  is a so-called band-matrix with non-zero values only at and around the main diagonal.

The basis was taken for  $l$  from 0 to 50 with restriction on  $m = 0$ . The results will be presented later in the experimental part to compare them with experimentally measured resonances and those calculated from analytic formulae (1.47).

## 1.4 VLD profile

To obtain a correct VLD profile, i.e.,  $L$  as a function of the radius  $r$ , is not easy due to the high complexity of the He II flow. Based on the steady solution of the Vinen equation (1.28) we can expect  $L \propto 1/r^4$ , since the counterflow velocity  $v_{ns} \propto 1/r^2$ . This approach has several issues. The specific dynamics of vortices in the counterflow is not fully included, neither is the generation and decay of vortices on the surface of the heater. The question of the generation and decay on the surface is proposed by Holm [24] and it would require deeper analysis.

From numerical simulations, made by Tsubota [9] or by the Newcastle group [12] in the cylindrical geometry, a vortex shell forms in the vicinity of the heater with maximum density in some non-zero distance from the surface. From the recent simulation by our group member Róbert Jurčo, we observe the dependence  $L \propto 1/r^4$ , see Figure 1.6 with no such pronounced maximum, likely due to known shortcomings of the model.

The temperature profile can have an effect on the vortex distribution as well. Due to the temperature maximum at the heater, the counterflow velocity is affected and we can expect a deviation from  $L \propto 1/r^4$ .

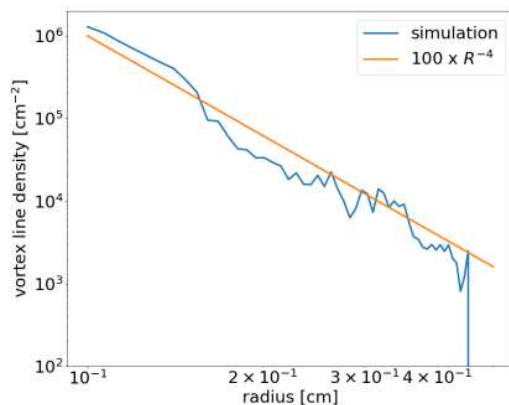


Figure 1.6: Result of the numerical simulation based on the Vortex filament model, we observed the dependence  $L \propto 1/r^4$ . Taken from Jurčo's Bachelor's Thesis.

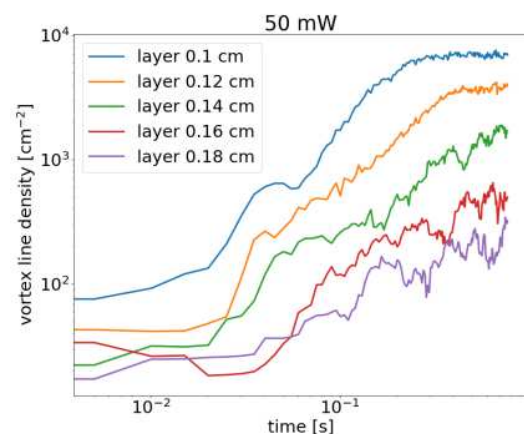


Figure 1.7: Gradual development of steady state VLD in different spherical layers. Taken from Jurčo's Bachelor's Thesis.



# 2. Experimental apparatus and control

## 2.1 Cryostat and cooling

Our experiment was realized in a 60 l cryostat made by Precision cryogenics, consisting of a cylindrical helium bath surrounded by an isolation shell. The shell is filled with a shielding material, which prevents heat fluxes and radiation from surroundings and is pumped to a vacuum. The outer face of the cryostat is made of steel, providing resistance to possible overpressure or mechanical damage.

The experimental cell was mounted on the cryostat insert, a system of metal tubes and flanges, which serves as a construction for attaching all experimental components, including thermometers and wiring. The upper part of the insert has holes for connections to pumps, a barometer and a siphon. The siphon is used to transfer the liquefied helium from a transport Dewar-vessel. Liquid helium is transported from the liquefier, located in the Cryogenics pavilion (same as our laboratory).

Since we need to lower helium temperature, the pumping system is connected to the cryostat. During an experiment, saturated vapours are continuously pumped. This reduces temperature or keeps temperature stable in equilibrium with a possible heat flux to the bath. In our experiments, we use two serially connected pumps. The first is a classical rotary vane pump, which is used to pump the boiling helium at 4.2 K, to the superfluid state and lower the temperature to cca 1.65 K. For reaching a lower temperature than 1.65 K a more powerful pump is necessary, in our case the Roots pump is switched on. This pump is oil-free and the principle of its running is different, since two rollers, having a shape of the number eight, co-rotate in a pump chamber and transport the helium gas.



Figure 2.1: Helium cryostat used for measurements.

## 2.2 Temperature control

The temperature of liquid helium can be deduced from the saturated vapour pressure (SVP), which works like a semi-primary thermometer. Values of SVP against the temperature are well-known [16] and does not depend on an experiment. SVP is tracked using the MKS Baratron, consisting of a measuring head (model 690 A) directly connected with the cryostat by a tube and a readout unit (model 670 C) ranging from 0 to 1000 Torr.

We installed different types of resistive thermometers useful in different temperature ranges to observe the current temperature. During a pre-cooling process by cold helium vapour from the Dewar flask, the Pt-100 thermometers in the upper, middle, and lower of the cryostat were used. At helium temperatures (4.2 K and lower), the dependence of the Pt-100 resistivity on the temperature is too weak, since temperature-independent crystallographic defects begin to play the main role in the limitation of electron transport. For these low-temperature ranges, we used semiconducting germanium or gallium arsenide, TTR-G thermometers by the Microsensor company, which provide reasonably good accuracy. One of these thermometers was located in the helium bath and one directly in the experimental cell. Both thermometers were connected 4-point by brass wires in the CuNi coating to the temperature-controller Lakeshore 340 and during the cooling calibrated. After calibration, their operative range was between 1.25 K and 3.00 K.

Stabilization of temperature was secured by a PID-algorithm with a regulation  $40 \Omega$  heater (manganin wire) in the  $^4\text{He}$  bath. The power applied to the bath by the heater is given by the following formula:

$$\dot{Q}(t) = P(T_0 - T(t)) + I \int_{t_0}^t (T_0 - T(t')) dt' + D \frac{d}{dt} (T_0 - T(t)). \quad (2.1)$$

How the coefficients  $P, I, D$  are chosen usually depends on experimental conditions, for example, on the pumping rate, which is in fact a counter-effect. The terms in brackets  $T_0 - T(t)$  actually mean a current error of the bath temperature, since  $T(t)$  is a current measured temperature and  $T_0$  is the set-point. In our case,  $T(t)$  was detected by the TTR-G thermometer in the bath. The implementation of PID was made in the programming environment LabVIEW.

## 2.3 Second sound sensors

The role of the Second sound sensor (SS sensor) was outlined in the theoretical part when we spoke about the numerical calculation of Second sound resonances 1.3.2. Such a sensor consists of a brass electrode in the shape of a cylinder with 3 mm in high and 7.5 mm in diameter, and for superfluid component permeable membrane, which is from one side gold-plated with 20 to 60 nm of gold. The membrane is stretched on the electrode and conductively connected to the body of the experimental cell. The SS sensor can be considered a capacitor. To increase the capacitance of the SS sensor, the electrode is pushed against the membrane by a spring. The capacitance is inversely proportional to the distance between

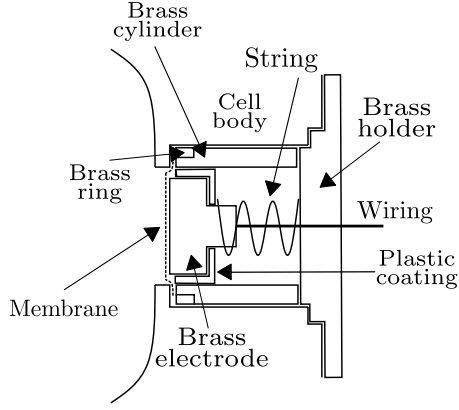


Figure 2.2: The sketch of the second sound sensor and its placement in the cell body.

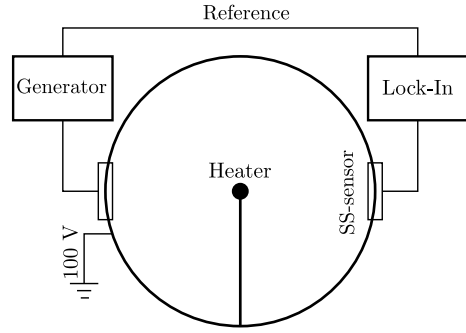


Figure 2.3: The scheme of the experiment arrangement.

plates. The detailed scheme of the used SS sensor and its attachment in the cell body is in Figure 2.2.

A pair of SS sensors is needed in the experiment, the transmitter and the receiver. A DC voltage bias is applied to the body of the spherical cell, respectively to electrodes. To induce the SS waves, we must get the transmitter membrane to oscillate, which is caused by AC voltage applied to the electrode. Since the membrane is not permeable for the normal component, the components of He II will oscillate with opposite phases. These waves inevitably force the receiver membrane to oscillate in a similar way, which causes the inducing of a detectable voltage.

The Agilent generator 33250A supplied an AC voltage, and the resulting signal from the receiver was detected using a phase-sensitive amplifier Lock-in Stanford Research SR-830. To suppress frequencies differing from the frequency of a generating signal, the Lock-in takes a reference signal from the generator. The product of the Input-signal from the receiver and the reference signal is then integrated with the time frame given by time-constant  $\tau$ , which is related to a cut-off frequency as  $f_{cut} \propto 1/\tau$ .

## 2.4 Spherical resonator

We developed a new spherical resonator/cell for our experiment, which should fulfill the spherically symmetric counterflow requirements. The cell was sketched in a free-downloadable Free-CAD program and manufactured from brass. The whole construction consists of three parts – two are identical, and the third is a joint between them, see Figure 2.4. The two identical parts constitute the inner spherical cavity with the radius 10 mm. This dimension was chosen considering the SS resonance profile and possible radial dependence of VLD.

A pair of SS sensors is placed oppositely in holes on the poles of the hemispheres. Since the electrode has a flat surface, the geometry of the sphere is slightly disturbed with a deviation of approximately 0.5 mm. We do not expect it would have a significant effect on measurements, since the counterflow velocity at the cell's wall is very small as it drops as  $v_{ns} \propto 1/r^2$ . This leads to the

emergence of very few quantized vortices near the outer wall.



Figure 2.4: Photo of the completely disassembled cell.

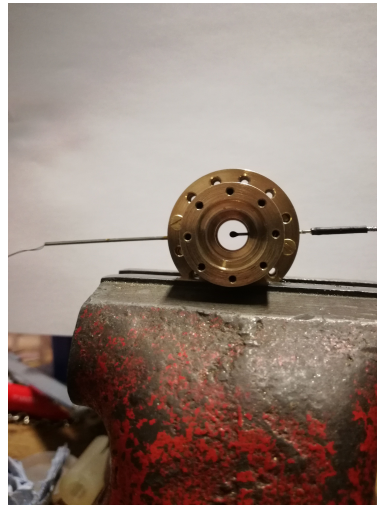


Figure 2.5: The side-photo of the cell with the heater and the capillary with wires to the TTR-G thermometer.

A heater is held in the middle of the cell by a small steel capillary. The heater is a small  $150 \Omega$  resistor covered by Stycast 2850FT epoxy (cca 1.8 mm in diameter), which should ensure approximately isotropic diffusion of heat. The capillary provides support for the heater itself and wiring – a brass conductor in CuNi sheath was chosen for thermal insulation. Another heater of the same type and resistance was placed in the helium bath, which allows the continuous switching between powers applied to the cell and the bath. This is crucial during a decay measurement. The power applied to the cell-heater was measured using a 4-point connection, i.e., knowing the current from the power supply and the measured voltage on the heater, the power can be easily calculated.

# 3. Results

## 3.1 Spherical resonances of second sound

We carefully mapped resonances of second sound in our spherical cavity. As the SS speed varies with the temperature, so do resonance frequencies. The optimal temperature for SS mapping is 1.65 K, since the dependence shows the local maximum, see Figure 1.4. The SS speed also grows steeply for temperatures lower than 1.0 K, but this range is not accessible in our experiment, and due to the low normal fluid density, the mechanical excitation of the SS wave would be almost impossible.

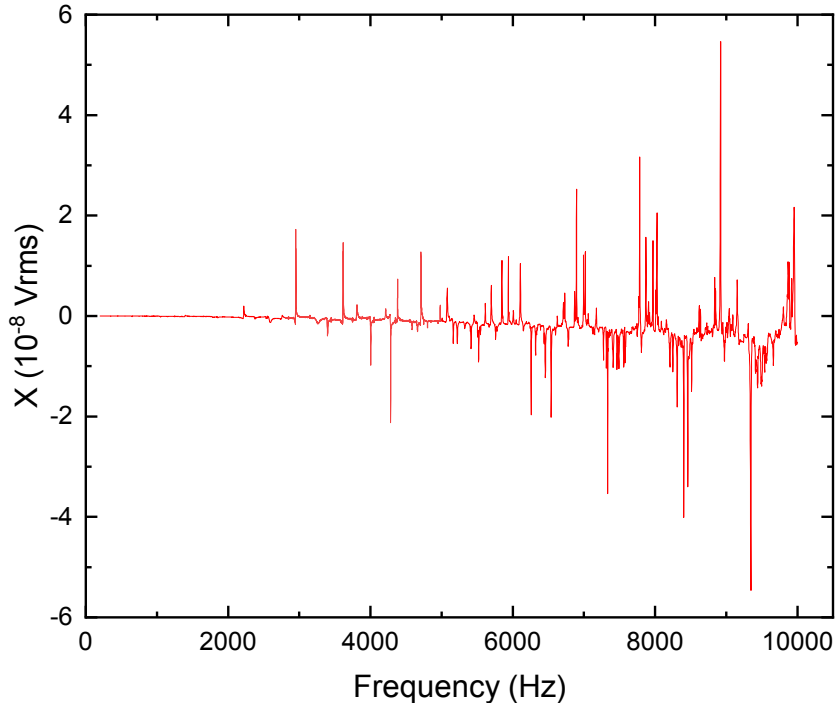


Figure 3.1: The frequency spectrum of the X-component of SS resonances in the spherical cell at 1.65 K between 0 kHz and 10 kHz. The spectrum becomes more complicated with increasing frequency, which is caused by degeneracy of the spherical harmonics with the number  $m$ .

The amplitude of the resulting signal  $x_0(\omega)$  has two components: dispersion and absorption, which are phase-shifted by  $\pi/2$ . Since the damping is linear, these components can be in the complex notation described as:

$$x_0(\omega) = f_0 \frac{(\omega_0^2 - \omega^2) - i\gamma\omega}{(\omega_0^2 - \omega^2)^2 + \gamma^2\omega^2}, \quad (3.1)$$

where  $\omega$ ,  $\omega_0$ ,  $\gamma$  and  $f_0$  are respectively the angular frequency of the driving signal, the resonance angular frequency, the damping factor and the amplitude of the driving force (in our case, this force is proportional to the AC voltage).

In the following, taking into account (3.1), we will consider the dispersion as a real Y-component and the absorption as an imaginary X-component, as Lock-In measures it. Usually, these components have an additional phase shift with respect to the Lock-In, therefore a phase correction must be set on the Lock-In to measure the X-component as purely absorptive.

We sought resonances up to 10 kHz. The frequency spectrum, driven by 7 Vrms (the root mean square voltage, the amplitude of the initial signal divided by  $\sqrt{2}$ ) at 1.65 K without the phase-correction, is in Figure 3.1.

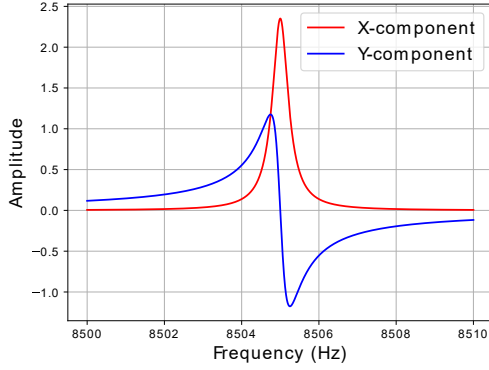


Figure 3.2: Typical shape of the X and Y-component, i.e., so-called Lorentzian curves described by (3.1).

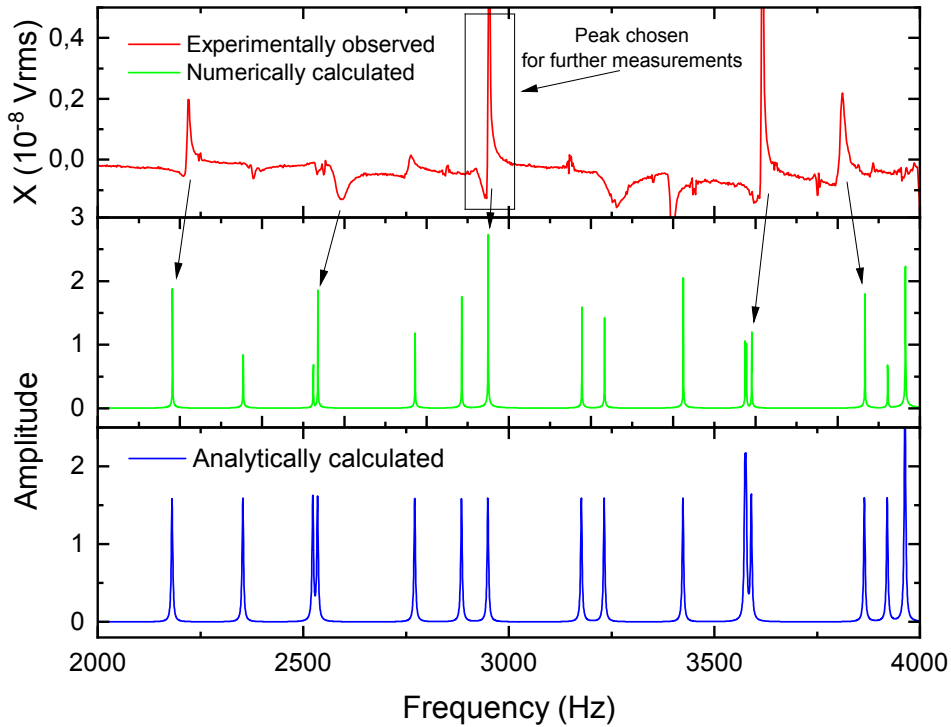


Figure 3.3: Experimentally observed resonance spectrum for frequencies between 2 kHz and 4 kHz in comparison with numerically and analytically (1.47) calculated values for  $R_1 = 0.9$  mm and  $R_2 = 10.04$  mm at 1.65 K. The analytic calculation does not include the dissipation due to the surrounding medium. Arrows show corresponding peaks and black rectangle shows the resonance peak used for further measurements. The amplitude of calculated resonances is rather illustrative.

Additionally, we provide a comparison of measured resonances with theoretical calculations mentioned in the Section 1.3. Two regions were chosen, with lower frequencies between 2 kHz and 4 kHz and with higher frequencies between 8 kHz and 9 kHz, to demonstrate the splitting, which is more apparent at high frequencies. The resulting spectra are in Figures 3.3, 3.4.

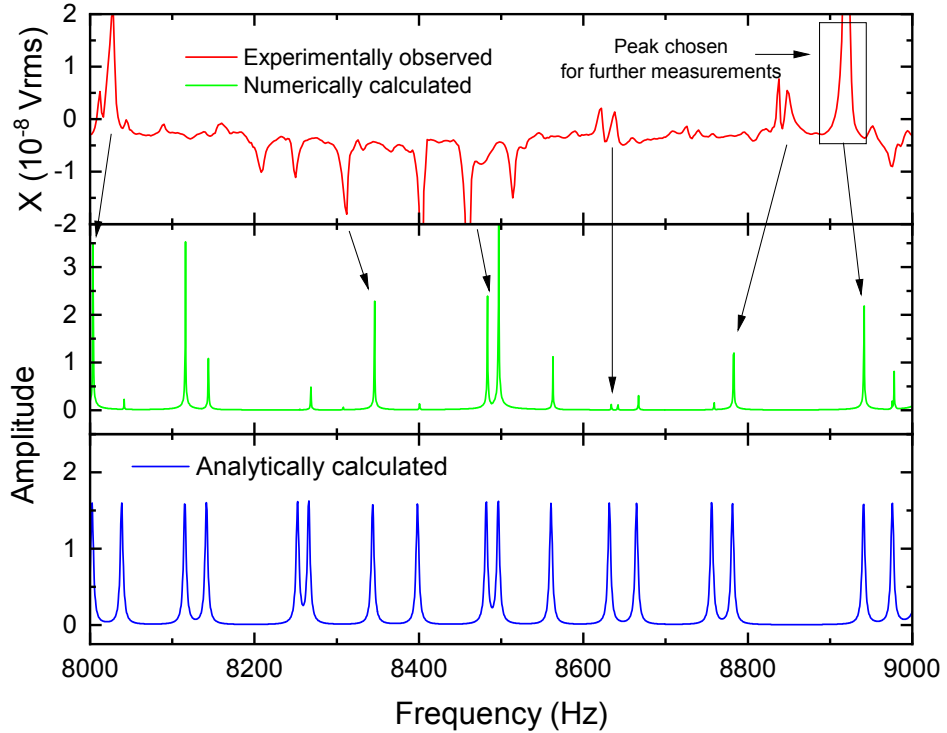


Figure 3.4: Experimentally observed resonance spectrum for frequencies between 8 kHz and 9 kHz in comparison with numerically and analytically (1.47) calculated values for  $R_1 = 0.9$  mm and  $R_2 = 10.04$  mm at temperature 1.65 K. The analytic calculation does not include the dissipation due to the surrounding medium. Arrows show corresponding peaks and black rectangle shows the resonance peak used for further measurements. The amplitude of calculated resonances is rather illustrative.

We see the numerically calculated (the calculation based on the basis decomposition) peak positions generally agree with the measured mainly in the lower frequency region, but they still show some shifts. These shifts are caused by uncertainty in boundary conditions, since the presence of the capillary is not included in calculations, similarly to the perturbation caused by flat SS sensors or deviation from the perfect sphere. Also, the damping can affect results, since the real damping is higher than in the numerical calculation. The measured spectrum can contain not only second sound resonances but also resonances from other sound modes, and some second sound resonances do not have to be detectable due to the sensor geometry and the angular dependence of the resonance profile. This angular dependence likely causes deviations in the high frequency range. The radii  $R_1$ ,  $R_2$  were optimized in calculations to get the best agreement

between calculated and measured resonances.

Looking only at theoretical values, we can compare results obtained numerically and analytically<sup>1</sup>. For the numerical calculation, the basis was chosen from  $l = 0$  to 50 and for the analytical only to 20, since we observed the frequencies from higher  $l$  lie over 9 kHz. We see really good agreement, although the analytic calculation (1.47) does not include the correct damping. The analytically calculated values are in Table 3.1.

$l/n$	1	2	3	4	5	6	7	8
0	1457	2523	3589	4665	5749	6839	7935	9034
1	670	1909	<b>2949</b>	3963	4978	6008	7053	8115
2	1079	2352	3423	4460	5478	6484	7487	8496
3	1457	2771	3865	4920	5958	6985	8002	9009
4	1823	3176	4292	5362	6411	7451	8481	9506
5	2180	3574	4709	5794	6854	7901	<b>8940</b>	-
6	2534	3964	5151	6219	7288	8343	9390	-
7	2884	4349	5525	6637	7718	8781	-	-
8	3231	4730	5926	7050	8141	9213	-	-
9	3577	5106	6322	7459	8560	9639	-	-
10	3920	5481	6714	7864	8975	-	-	-

Table 3.1: Table of analytically calculated frequencies (1.47) up to 10 kHz at 1.65 K with boundary conditions  $R_1 = 0.9$  mm and  $R_2 = 10.04$  mm. Rows denote the order of the spherical Bessel function  $l$ , and columns denote roots  $n$  of the corresponding function. We coloured the values corresponding to the resonances used for measurement.

From the measured spectrum, we chose two frequencies suitable for SS attenuation measurements 2950 Hz and 8923 Hz. The main factors speaking for this choice were that no adjacent peak perturbs the chosen peak and its Q-factor is high enough (higher than 1000). The lower peak had the Q-factor 1280 and the higher 1720. According to the table 3.1, we see these frequencies should correspond to calculated values 2949 Hz ( $l = 1$ ,  $n = 3$ ) and 8940 Hz ( $l = 5$ ,  $n = 7$ ).

As we know the resonance frequency, the resonance wave number  $k_{ln}$  and the boundary conditions, we can easily obtain the profile of the undamped resonance in the cell as a radially dependent function:

$$\Phi(r) = \alpha_l \left( j_l(k_{ln}r) - \frac{j_l'(k_{ln}R_1)}{y_l'(k_{ln}R_1)} y_l(k_{ln}r) \right), \quad (3.2)$$

where  $\alpha_l$  can be chosen arbitrarily, since it has the role of a scaling parameter. Profiles are in Figure 3.5.

As we shall see, resonance profiles have different numbers of maxima, two and six. This can have an effect on vortex detection. The sensitivity of the resonance profile to the vortex tangle is proportional to the square of the amplitude, i.e.,

<sup>1</sup>For clarity, roots of the analytic formulae (1.47) must also be found numerically. Still, the situation is different, since in the case of the basis decomposition, we numerically solve the whole problem, including solutions of proposed differential equations (1.56),(1.57).

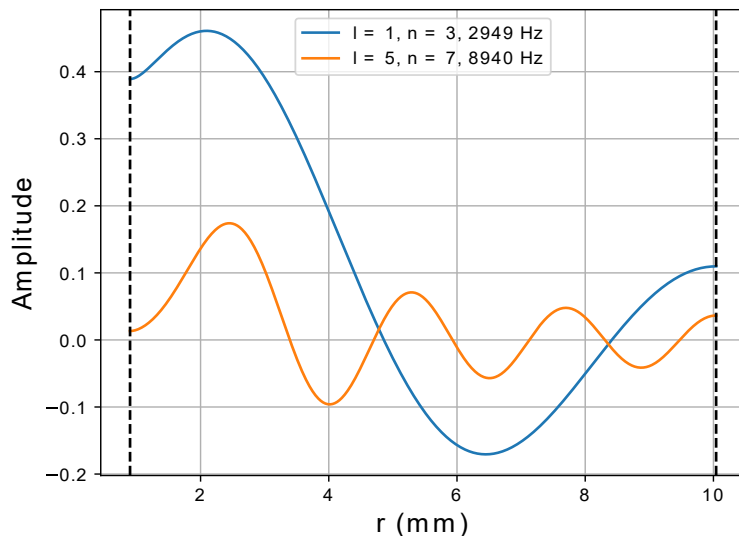


Figure 3.5: Resonance profiles at 1.65 K belonging to resonance frequencies chosen for further measurements. The dashed lines represent the surfaces of the heater and the spherical cell.

the most sensitive parts of the curve are in its extrema [8]. We will discuss this more later 4.1.

At the end of this section, we should mention the fundamental, the lowest resonance frequency/mode. This mode is observable at the frequency 670 Hz and corresponds to the first root of the first order function. We observed this mode too, but its quality was poor, since the multiples of network frequencies were present in the signal.

## 3.2 Cell overheating

Since we apply power to the heater in the middle of the spherical cell and the cell's body has a non-negligible thermal resistance, the temperature of He II can be higher than in the bath. This overheating causes shifts in the SS speed, i.e., in resonance frequencies, and affects the ratio between densities.

From 3.6 we see the overheating becomes apparent at powers higher than 20 mW, and the maximum difference is 60 mK at 170 mW. This causes the resonance frequency shift of approximately 0.3% with respect to the value measured at 1.65 K, and 1.8% at 1.30 K.

We can obtain the absolute thermal resistance of our cell as  $R_T = \Delta T / \dot{Q}$  and plot it against the power as it is in Figure 3.7.

A theoretical explanation of the observed behaviour is not straightforward. Two channels are present to transport heat from He II in the cell through the cell's body to the bulk. The first is heat conduction through the brass, described by Fourier's law:

$$\frac{\dot{Q}}{A} = -k\nabla T, \quad (3.3)$$

where  $k$  is the thermal conductivity. The thermal conductivity of brass is linearly

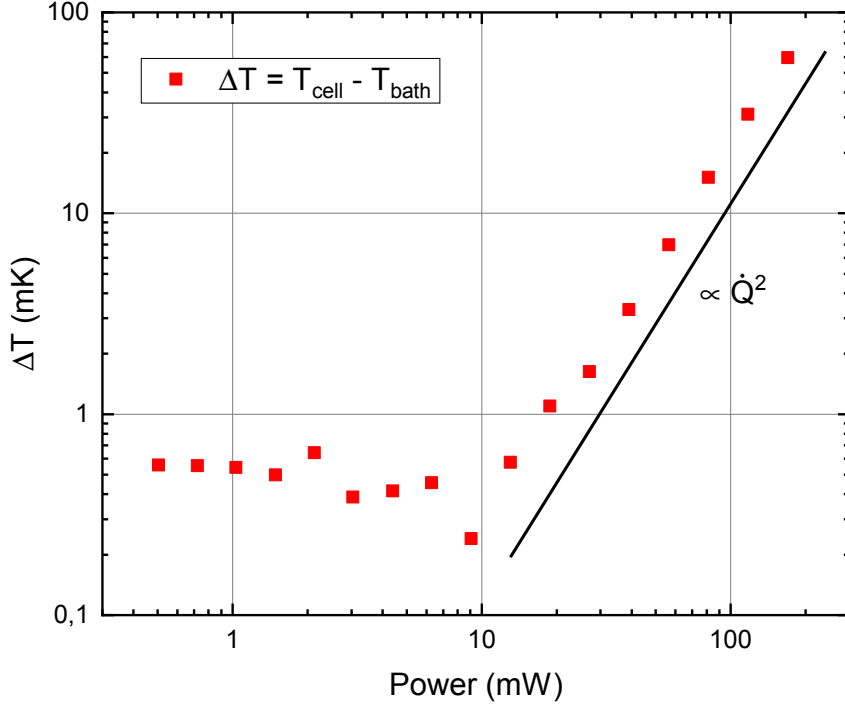


Figure 3.6: Difference between the bath temperature and the temperature in the spherical cell against the power applied to the heater. The bath temperature, i.e., the temperature at infinity, was stabilized at 1.65 K with the shift of approximately +2 mK at the highest power (by constant pumping rate using the PID algorithm). Values for powers lower than 10 mW are affected by the uncertainty of the thermometer’s calibration, estimated as  $\pm 1$  mK. For powers higher than 10 mW,  $\Delta T$  is clearly proportional to  $\dot{Q}^2$ .

proportional to the temperature  $k \propto T$  at  $T < 10$  K, since only the conduction electrons contribute to the heat transfer. For small  $\Delta T < 0.1$  K,  $k$  can be considered as constant of the magnitude approximately 1 W/(m · K) (taken at 1.65 K) [25]. This corresponds to a thermal resistance of  $\approx 3.3$  K/W.

The second is the heat transfer thanks to He II flowing through leaks in the cell’s part junctions. As we know, He II has an extremely high thermal conductivity several orders of magnitude higher than brass, therefore this contribution is non-negligible. For He II the phenomenological Gorter-Mellink relation [26] was obtained:

$$\left(\frac{\dot{Q}}{A}\right)^3 = -\tilde{k}\nabla T, \quad (3.4)$$

where  $\tilde{k}$  is the effective thermal conductivity of He II with the magnitude  $\tilde{k} \gg k$ .

What we should expect is  $\Delta T \propto \dot{Q}$  from (3.3) and  $\Delta T \propto \dot{Q}^3$  from (3.4). Since the observed behaviour is  $\Delta T \propto \dot{Q}^2$ , we can assume an interplay between both heat channels. Nevertheless this problem would require deeper analysis with respect to the geometry of the whole cell.

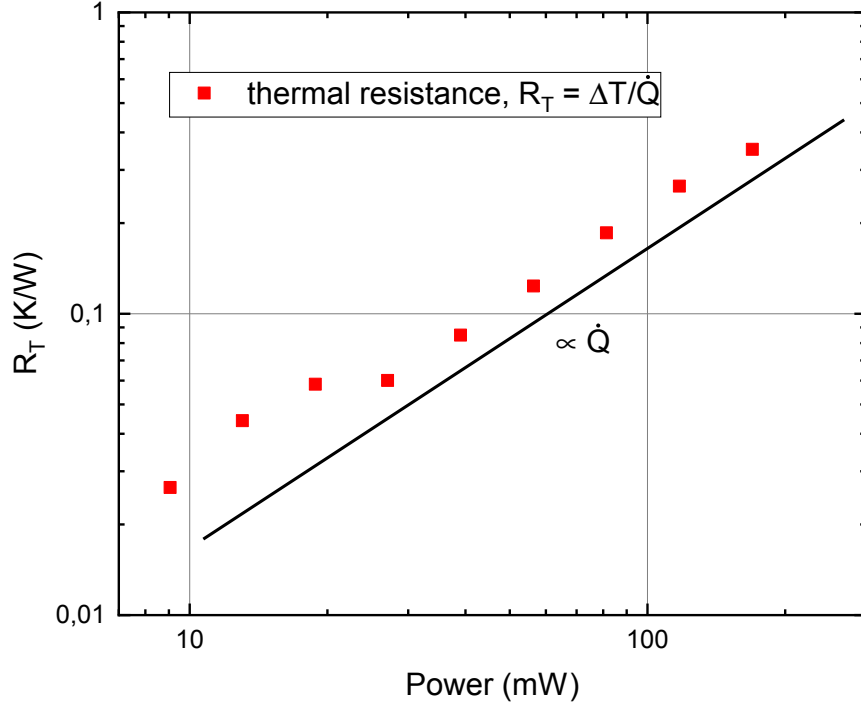


Figure 3.7: Dependence of the thermal resistance  $R_T$  on applied power  $\dot{Q}$  together with the black line indicating  $R_T \propto \dot{Q}$ . At bath-temperature 1.65 K.

### 3.3 Temperature profile measurements

The temperature profile is essential for the existence of the steady state turbulence in the thermal counterflow as follows from calculations in cylindrical geometry [11], which show that without a temperature gradient steady solutions cannot be obtained.

The measurement was performed directly in the helium bath. We designed a holder for three TTR-G thermometers (one of them was subsequently used in the cell) and the heater, which could move vertically. The holder was 3D-printed from PLA (polylactic acid) with copper nano-particles. The heater was again a small resistor covered by silver-epoxy creating a sphere with 2 mm in diameter – silver nano-particles should ensure better heat conductivity. This experiment took place in the same cryostat with the same pumping system and thermometer as we described above 2.1.

The measurement ran as follows: We periodically change between two distances, one near the heater at well-defined distance and one far from the heater. This vertical movement was realized by a stepper motor. The temperature was continuously measured by previously calibrated thermometers. The results are plotted in Figure 3.9.

We see the temperature difference caused by the thermal counterflow is very small, hundreds of  $\mu K$ , and since it falls with the radius as  $1/r^p$ , where  $p$  is between 5 and 6, the profile is evident only up to 1 mm or 2 mm from the heater

surface. We can treat this effect as negligible in comparison to the overheating of He II in the cell, but taking into account the temperature dependence of  $v_{ns}$  (1.25) and  $L \propto v_{ns}^2$ , the final distribution of VLD can be affected by the temperature profile.

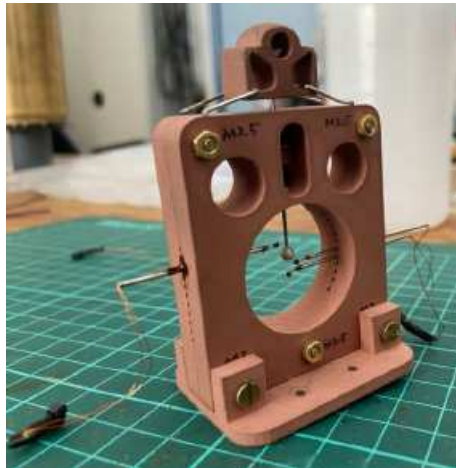


Figure 3.8: 3D-printed holder used for the temperature profile measurement. Three TTR-G thermometers are placed horizontally and the resistive heater vertically. Taken from Ref. [21].

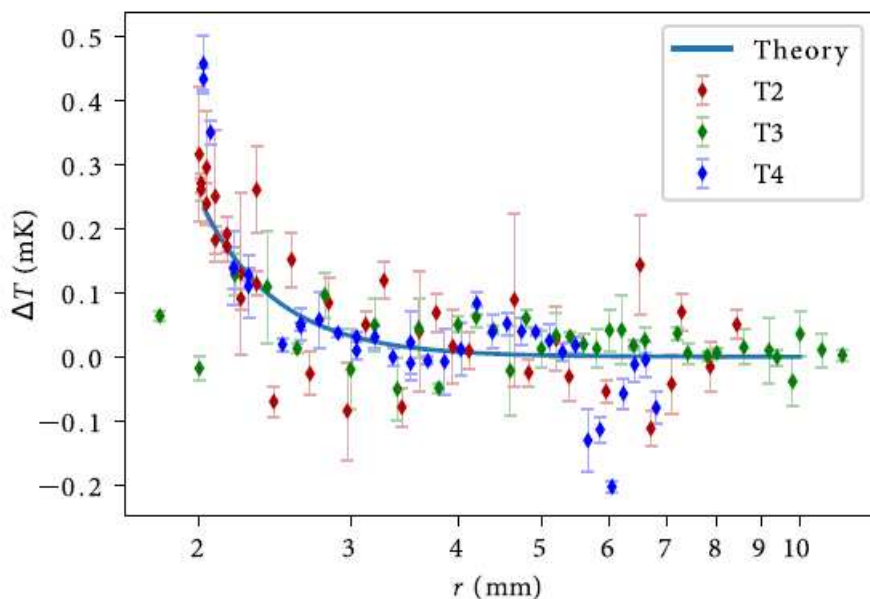


Figure 3.9: Results of the temperature profile measurement, i.e., the temperature difference between the temperature in the vicinity of the heater measured by three TTR-G thermometers and the bath temperature 1.50 K. The applied power to the heater was 500 mW. Experimental data are compared with the theoretically obtained dependence as the numerical solution of (1.39). Taken from Ref. [21].

We obtained an agreement regarding the comparison of experiment and theory, although the experiment requires high sensitivity of used thermometers, which are significantly affected by electronic noise.

*Particular acknowledgement to dr. Yunhu Huang and dr. Zhuolin Xie from the Department of Low Temperature Physics, who performed and planned the experiment during tough Covid-times.*

### 3.4 Steady state turbulence

We investigated the amount of vortices, characterized by the mean vortex line density (VLD,  $L$ ), in the spherical cell generated via continuously driven counterflow, which led to the emergence of a steady state. We used the second sound attenuation method to obtain  $L$  calculated from the relation (1.42). We note that strictly speaking, this relation works only for homogeneous vortex tangles. As a consequence, our values of vortex line density need not be numerically accurate, but scaling laws ought to be represented clearly. The attenuated amplitude is taken with respect to the unattenuated – measured without the presence of quantized vortices, at zero power. As we mentioned above, we chose two resonance frequencies 2950 Hz and 8923 Hz (1.65 K). We decided to perform this measurement at different He II temperatures: 1.30 K, 1.45 K, 1.65 K, 1.80 K and 1.95 K. The ratio between the normal and superfluid density is different at every temperature, which means a different effect on the flow due to the presence of the mutual friction force.

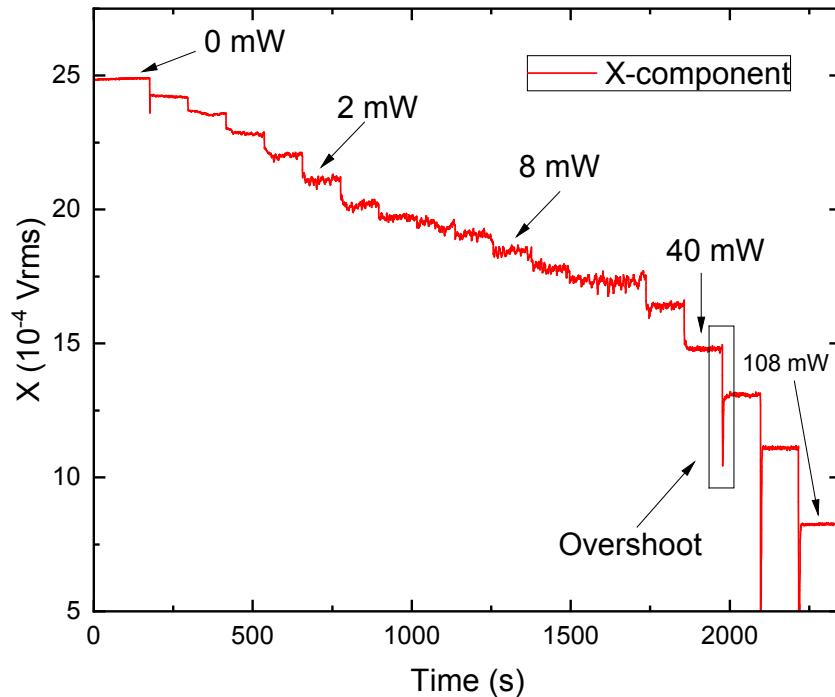


Figure 3.10: Typical data collected by tracking the resonance peak. Individual stairs belong to different powers applied to the heater. At higher powers, significant overshoots are present due to the limitation of the PID algorithm.

We accomplished the steady state measurement in two different ways. The first way is to collect the full frequency spectrum around the studied peak, called the frequency sweep. This peak is then fitted by a linear combination of Lorentzian (3.1) and Gaussian shape, so-called pseudo-Voigt peak, with consideration of a linear background. The final amplitude of the peak, used for VLD calculation, is then composed of two contributions  $A = \sqrt{X^2 + Y^2} + A_G$ , where X,Y are amplitudes of the absorptive and dispersive component and  $A_G$  of the Gaussian part.

The second way is to use continuous tracking of the resonance peak maximum. This is ensured by a PID algorithm set to keep the ratio Y/X near zero, since the amplitude of the Y-component is zero when the X-component is at its maximum. All values of the X-amplitude recorded during some time frame are corrected with respect to the linear background and time-averaged.

In Figure (3.11) we present data collected using the tracker and the frequency sweeps. They show reasonably good consistency at all temperatures and both frequencies. In further analysis, we constrain ourselves only to data from the tracker, since they underwent statistical averaging, so we can consider them accurate enough. We will present vortex line density against different quantities characterizing the flow.

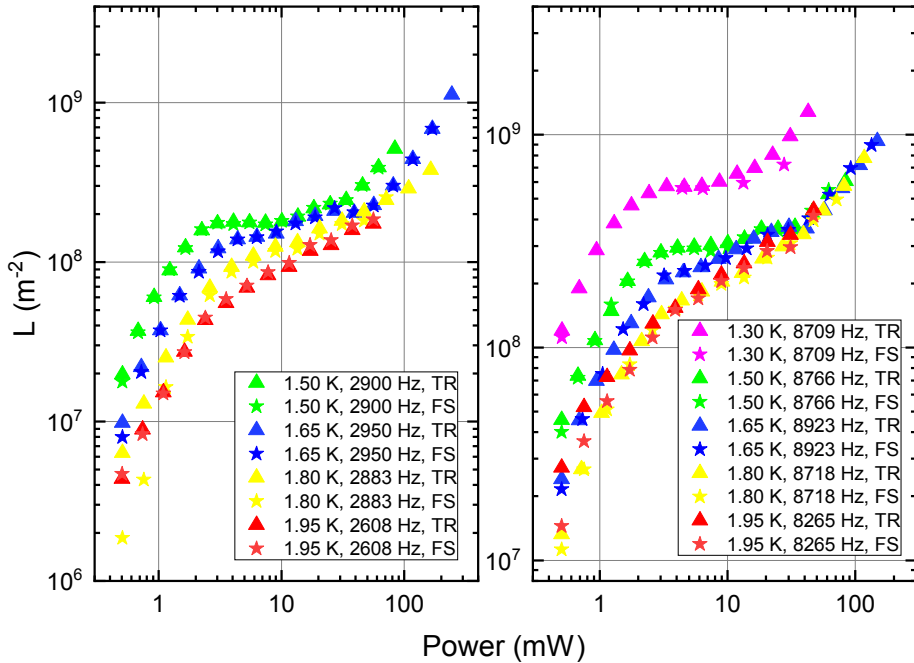


Figure 3.11: Vortex line density  $L$  against power applied to the heater measured at the lower and higher resonance frequency. TR denotes data from the tracker and FS from the frequency sweeps.

The dependence of VLD against power  $\dot{Q}$  represents raw experimental data, because  $\dot{Q}$  is a control parameter. On the other hand, it does not tell us much about the properties of the turbulent flow. Nevertheless, looking at Figure 3.12 we can deduce some basic characteristics of turbulence driven by the spherically sym-

metric counterflow. VLD clearly increases with decreasing temperature, which can be explained by higher  $v_{ns}$  at the same power due to the lower normal component density  $\rho_n$ . This behaviour is good to see also in previous two Figures. The second, more interesting observation is that the lower resonance frequency (2950 Hz at 1.65 K) detects less quantized vortices at a given temperature than the higher mode (8923 Hz at 1.65 K). This is probably an interplay of two effects, the profile of resonant curve in the cell 3.5 and the spatial distribution of VLD 1.4. We note that measurements with higher harmonic modes with a dense profile tend towards the average vortex line density in the experimental volume [8].

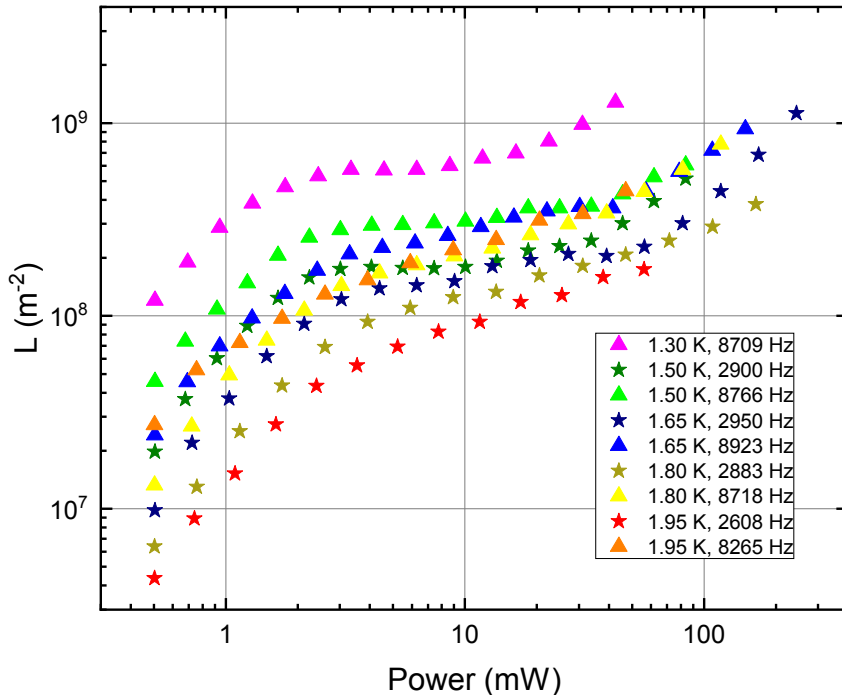


Figure 3.12: VLD against power, at bath temperatures between 1.30 K and 1.95 K for both resonance frequencies.

Next, we observed that the development of VLD on  $\dot{Q}$  does not possess any clearly defined dependence. The data does not coincide with what we expect from the Vinen equation (1.26) and that is  $L \propto \dot{Q}^2$ , since  $v_{ns} \propto \dot{Q}$ . We will discuss this together with the effect of the resonance and VLD profile later.

The counterflow velocity gives us a better idea of how strongly the flow drives the turbulence. We calculate the magnitude of  $v_{ns}$  at the distance  $r = 0.9$  mm, which should correspond to the surface of the heater. At the vicinity of the heater, the magnitude is the highest, since we know the velocity drops with the radius approximately as  $v_{ns} \propto 1/r^2$ . This is a significant contrast to the measurements in channels [8, 27, 28], where  $v_{ns}$  is constant along the whole channel.

From Figure 3.13 we see the VLD collapses to single dependence in certain regions, since  $v_{ns}$  reflects the physical properties of the whole system – temperature and geometry. We can divide these data into three main regions with respect

to  $v_{ns}$ , which depend on the resonance mode. The first region belongs to the velocities approximately up to 0.01 m/s, where VLD grows significantly with the counterflow velocity. The second region, say between 0,01 m/s and 0.07 m/s, shows slower growth of VLD than the previous one. In the third region, with velocities higher than 0.1 m/s, VLD again displays an evident increase. The data tend to grow together. Higher  $v_{ns}$  were unattainable due to the overheating causing significant shifts in resonance frequencies, beyond the capacity of the PID regulator.

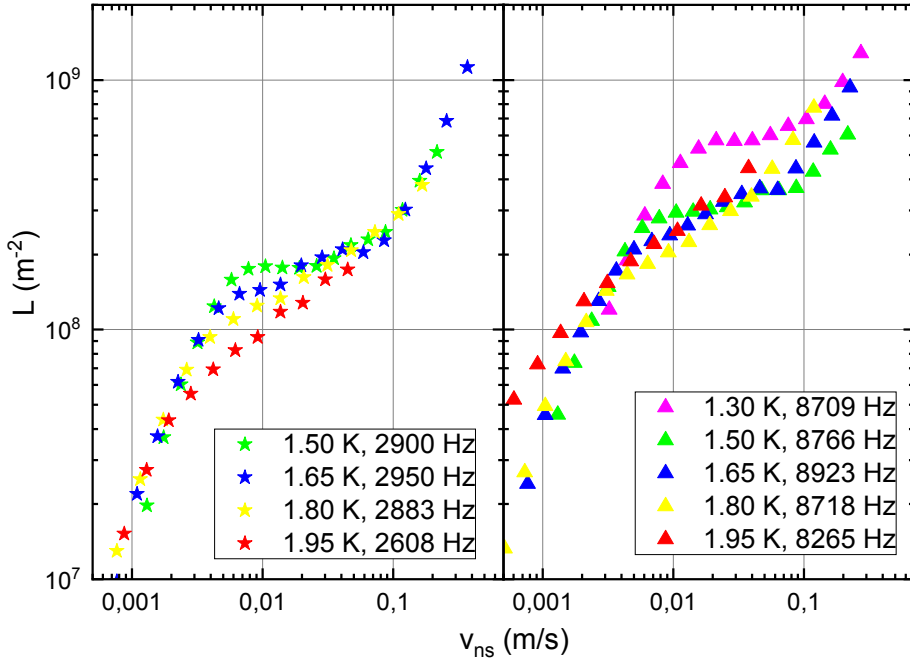


Figure 3.13: VLD against the counterflow velocity calculated at  $r = 0.9$  mm for different bath temperatures.

The crossing between the data in the first and second regions, respectively the very existence of the middle slowly growing region, is not presently understood. We hypothesize that it can be caused by turbulence in the normal component. To assess this phenomenon better, we shall use a parameter characterizing the flow of the normal component alone, the Reynolds number given as:

$$\text{Re}_n = \frac{v_n D}{\nu_n}, \quad (3.5)$$

where  $v_n$  is given by (1.24),  $D$  is a characteristic length-scale, we will take the radius of the heater surface  $R_1$ , and  $\nu_n$  is the normal component kinematic viscosity.

In Figure 3.14 we see that data are still divided into three regions when the slowly growing part starts at the Reynolds number around 40 or 50. At such values of  $\text{Re}_n$ , the non-linearities, originating from the convective term in (1.5), can occur, breaking the laminar flow. The emerging normal fluid turbulence could affect turbulence in the superfluid component. When we omit energy loss due

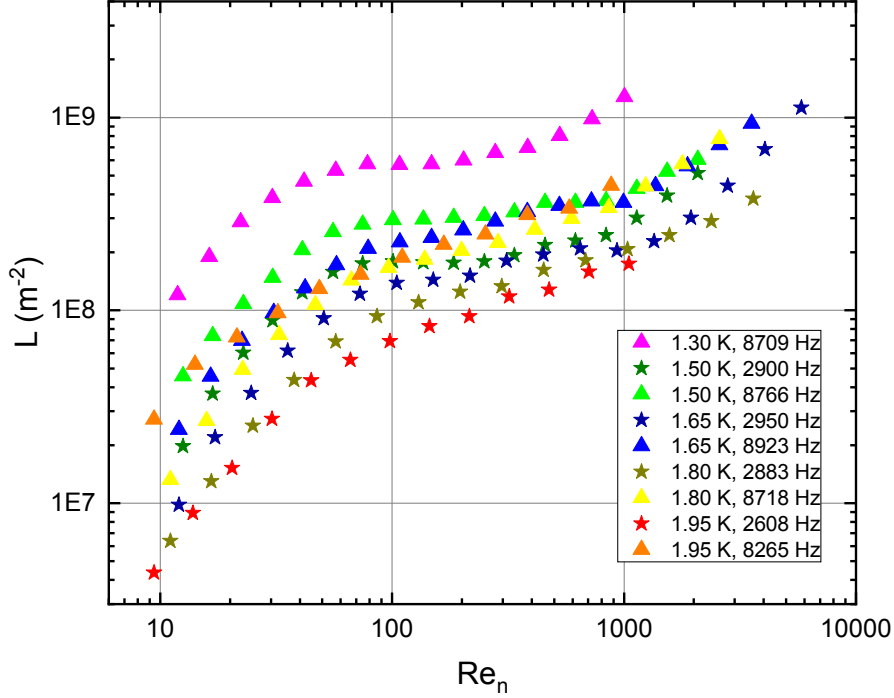


Figure 3.14: VLD against the normal component Reynolds number  $Re_n$  calculated for  $D \equiv R_1 = 0.9$  mm for different bath temperatures.

to evaporating or overheating, we can consider an energy exchange between the classical and the quantum turbulence in He II. The proposed theory is outlined in Chapter 4.2.

From  $v_{ns}$  and  $L$  we can deduce the parameter  $\gamma$  defined by the relation (1.28), which follows from the Vinen equation (1.26). This parameter should be only a function of the temperature through the mutual friction coefficient  $\alpha$ . This means  $\gamma$  should be constant at given temperature. We can compare our measured  $\gamma_{sph}$  with that observed in channels that satisfies  $\gamma_{ch}(s/cm^2) = 155.8T - 75.0$ . We present the ratio  $\gamma_{sph}/\gamma_{ch}$  in Figure 3.15, where  $\gamma_{sph}$  is easily calculated from measured  $L$  as  $\sqrt{L}/v_{ns}$ .

We see the temperature dependence is slightly suppressed at both resonance frequencies, but  $\gamma_{sph}$  is not constant. It differs significantly from that in the channel and depends on the used resonance frequency. The ratio is constant only at very low velocities, around 0.001 m/s and lower, at least we can obtain an effective  $\gamma$ -factor in the cell as an average of this constant part and we get:

$$\gamma_{sph,1}^{eff} \approx 2.26\gamma_{ch} \quad \gamma_{sph,2}^{eff} \approx 3.41\gamma_{ch}. \quad (3.6)$$

The first value belongs to the lower resonance mode and the second to the higher. The fact that these two values are greater than unity suggests that a higher VLD is produced in the sphere than would appear in a channel with counterflow at the maximum velocity. This behaviour in the sphere is probably given by the absence of boundaries, which likely contribute to the vortex annihilation in the channel or by the flow inhomogeneity.

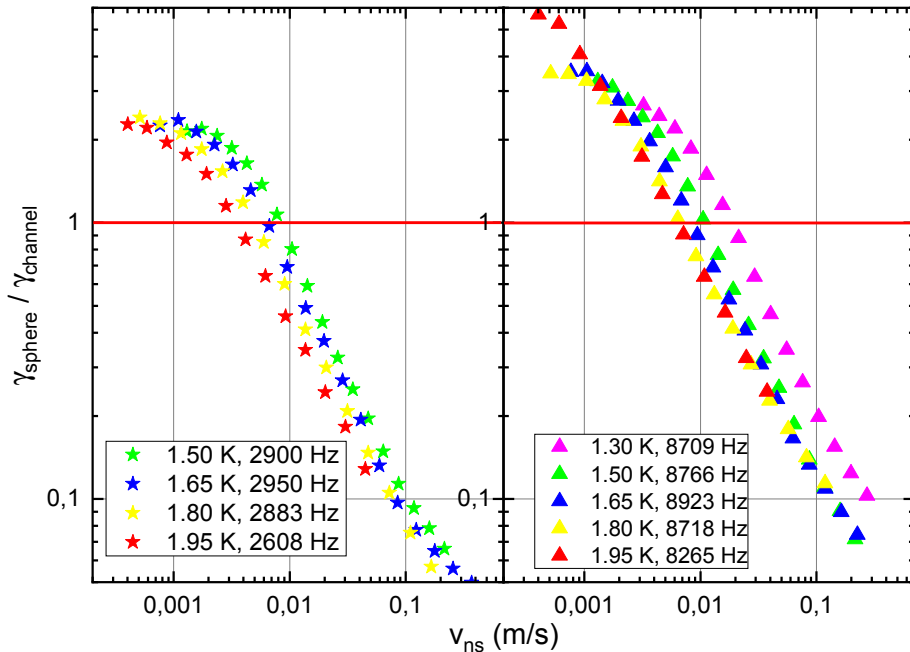


Figure 3.15: Ratio between the  $\gamma$ -factors observed in counterflow turbulence in channels and in the sphere against the counterflow velocity at both resonance frequencies.

We shall also briefly comment on the critical power/velocity for turbulence generation. In short, we did not clearly observe any, since at the lowest power  $\approx 0.5$  mW (counterflow velocity  $\approx 10^{-3}$  m/s) we measure a significant amount of vortices. Based on other experiments [8, 23], a critical velocity must exist, therefore we assume it is smaller than  $10^{-3}$  m/s in our case.

### 3.5 Decay of turbulence

Next, we studied the temporal decay of quantum turbulence after the heater is switched off. This can provide information about the conformation of the turbulent tangle in our spherical cell. After the heater is switched off, the energy is not further supplied to the turbulence (in general into turbulence in both components), and turbulent structures begin to decay. In the case of classical turbulence, they will undergo the Richardson cascade and afterwards dissipate energy due to viscous friction. In the case of quantum turbulence/vortices, they can lose energy through mutual reconnections, annihilation or by emitting phonons.

We performed the measurement using the tracker similarly to the steady state case. After the cell's heater is switched off, we needed the temperature in the cell not to change, therefore we applied the same power to the compensation heater in the bath. The time of turbulence generation, i.e., when power was applied to the heater in the cell, was approximately 100 s. After this time, the turbulent tangle should be fully developed and steady. Then we switched between the heaters and let the turbulence decay. The decay phase time was chosen between

300 s and 420 s depending on the used power. This sequence was repeated 50x and then averaged. We had to choose the used powers with respect to the bath temperature, since at high powers, say 50 mW and higher, the resonance frequency shifts a lot due to the significant cell overheating (already discussed above), which is more pronounced at low temperatures.

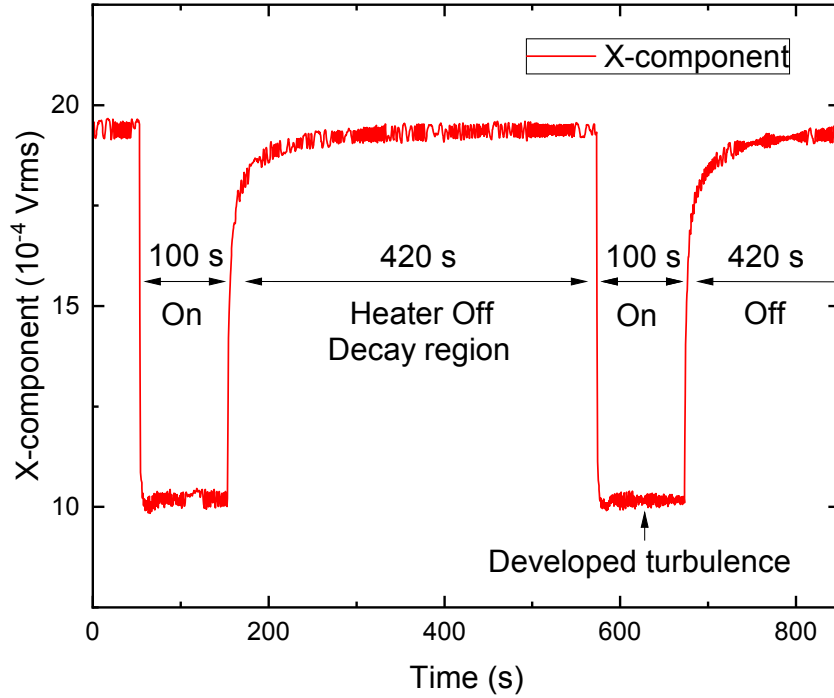


Figure 3.16: Example of the decay measurement sequence at 1.65 K with the power of 100 mW. The On/Off-regions show when the heater in the cell is working. In data processing, the regions with off-heater are separated from the signal and averaged.

From the averaged signal, the vortex line density (VLD,  $L$ ) is calculated using (1.42). The unattenuated amplitude is taken as a maximum from the last 50 points of the X-component from all signals (before averaging). To obtain a correct behaviour of VLD with time, we have to subtract the virtual origin time  $t_0$  and constant  $L_0$  characterizing remnant vortices remaining in the cell after the decay. The virtual origin time has a meaning of the time when VLD hypothetically begins to decay from infinity value, therefore it should be  $t_0 < 0$ . We obtained  $t_0$  by linear fit from the plot  $t$  versus  $1/L$  see Figure 3.17, the absolute term had the meaning of  $t_0$ . There is not an easy or a correct way how to obtain  $L_0$ , thus we estimated it directly from  $L$  versus  $t$  from the latest time values of  $L$ . The obtained  $L_0$  ranged between  $10^4 \text{ m}^{-2}$  and  $10^5 \text{ m}^{-2}$  depending on the individual dataset.

Final processed data are shown in Figures 3.18, 3.19, which differ in the used resonance mode as it is described in the Figure's captions. We shall see data generally agree with the decay mode  $L \propto 1/t$  following from the Vinen equation

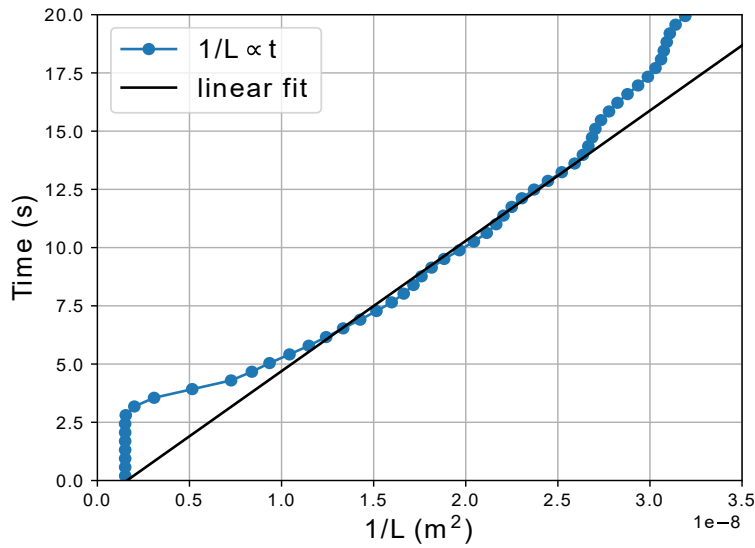


Figure 3.17: Typical way of obtaining  $t_0$  by the linear fit from the plot  $1/L$  against  $t$ .

(1.26). This dependence is strong mainly in the region of times between 50 s and 200 s. At earlier times we can observe some deviations. To judge something more accurate about times longer than 200 s is non-trivial, since data are affected by noise and the correct subtraction of  $L_0$ . In general, we do not observe any significant dependence of the decay on the used resonance mode, temperature or initial power.

The dependence, which we observe, is derived from the Vinen equation (1.26) with the assumption of homogeneous and isotropic turbulence. We should emphasize the initial vortex tangle definitely does not fulfill this assumption due to the presence of VLD profile 1.4. What exactly happens with a turbulent tangle after the heater is switched off is a question and we discuss it in 4.3.

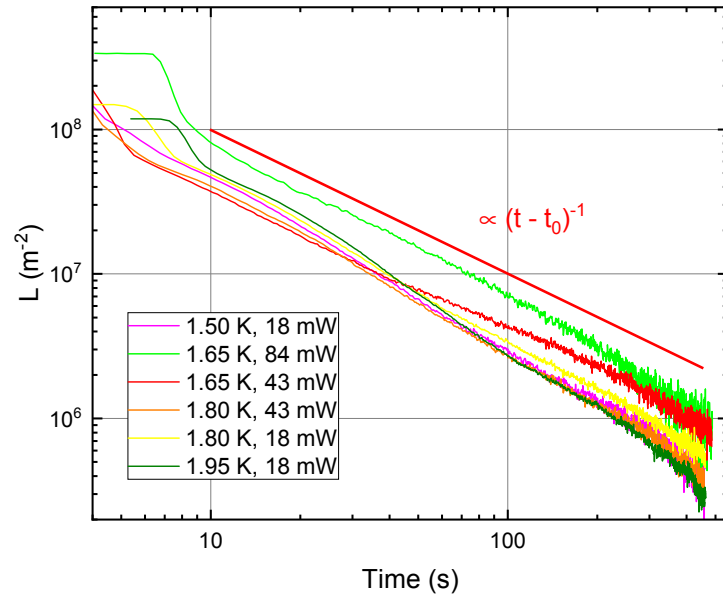


Figure 3.18: Decay measured at the lower resonance frequency (2950 Hz at 1.65 K) for different initial powers applied to the heater at bath temperatures. The red line characterizes the dependence  $L \propto 1/t$ .

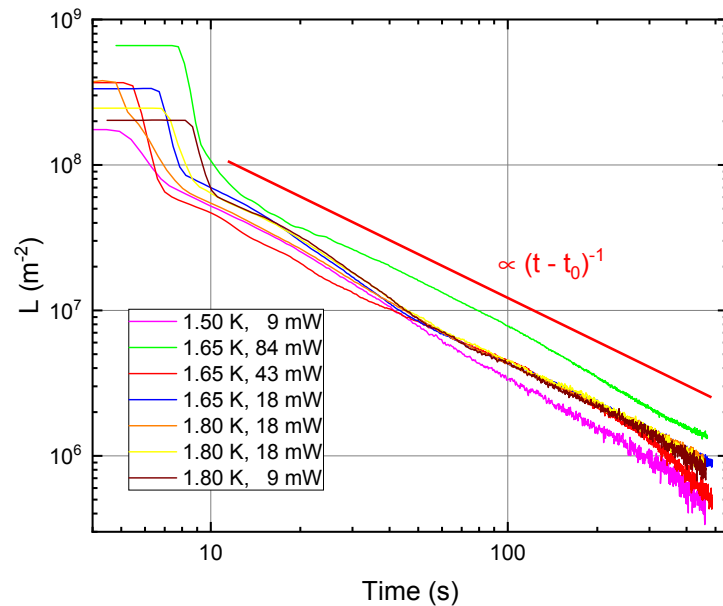


Figure 3.19: Turbulence decay measured at the higher resonance frequency (8923 Hz at 1.65 K) for different initial powers applied to the heater at different bath temperatures. The red line characterizes the dependence  $L \propto 1/t$ .



# 4. Discussion

## 4.1 VLD and resonance curve profile

As we know in the case of the homogeneous and isotropic quantum turbulence, we can derive from the Vinen equation (1.26) the dependence of VLD against the counterflow velocity  $L \propto v_{ns}^2$ . We mentioned above that our data behaves differently. Since we use the second sound attenuation and Equation (1.42), the measured VLD need not correspond to the actual density of vortex lines, but should approximate the mean VLD in the spherical cell. Under assumption of linear damping the measured VLD can be written as:

$$L = \frac{\int L(\mathbf{r})\Phi^2(\mathbf{r})d^3\mathbf{r}}{\int \Phi^2(\mathbf{r})d^3\mathbf{r}}, \quad (4.1)$$

where  $L(\mathbf{r})$  is the spatial distribution of VLD and  $\Phi(\mathbf{r})$  is the SS resonance curve profile. Detailed derivation of this relation with other comments is possible to find in the article [8]. We can further assume the simplest spatial distribution  $L = \gamma^2 v_{ns}^2 = A/r^4$ , where  $A = (\gamma\dot{Q})^2/(4\pi ST\rho_s)^2$ , and for simplicity only radially dependent resonance profile  $\Phi(r)$  given by the equation (3.2). We can substitute this into (4.1) and integrate in the spherical coordinates to obtain:

$$L = \frac{\int_{R_1}^{R_2} A\Phi^2(r)/r^2 dr}{\int_{R_1}^{R_2} \Phi^2(r)r^2 dr} = A \frac{I_1}{I_2} \propto \dot{Q}^2. \quad (4.2)$$

We see the result is still proportional quadratically to the power. It means that under the simplifying assumptions, the experimentally observed behaviour is not caused by specifics of the resonance profile or by the spatial distribution of VLD. But in reality  $L \propto 1/r^4$  is not satisfied exactly, especially close to the heater due to the presence of the temperature profile. This interpretation is also supported by the fact that the measured behaviour of  $L$  versus  $\dot{Q}$ , see the figure 3.12, does not depend on the resonance mode. At the same time we know that the used resonance modes are spatially completely different, whether we look at the number of extrema or at the much more complicated angular dependence of the higher mode ( $l = 1$  is connected to 3 different spherical harmonics and  $l = 5$  to 11).

## 4.2 Quantum and classical turbulence interplay

In the following, we will investigate our hypothesis that turbulence in the normal component can affect the density and motion of quantized vortices in the superfluid component, possibly being responsible for the slowly growing region at medium powers in Figure 3.13. Since the normal fluid velocity is proportional to the radius as  $v_n \propto 1/r^2$ , turbulent structures can occur mainly in the vicinity of the heater surface. To assess the flow properties of the normal component we can compare the magnitude of the non-linear convective term  $(\mathbf{v}_n \cdot \nabla)\mathbf{v}_n$  and the

viscous term  $\nu_n \Delta \mathbf{v}_n$ . The ratio of these terms is in fact a radially dependent Reynolds number, but we avoid this notation, as usually  $\text{Re}_n$  is understood to characterize a flow as a whole, not its local properties. We will remember the relation  $v_n = \dot{Q}/(4\pi s T \rho r^2)$  and define the prefactor  $\delta := 1/(4\pi s T \rho)$ , assuming constant  $s$ ,  $T$  and  $\rho$ . Then, we obtain:

$$(\mathbf{v}_n \cdot \nabla) \mathbf{v}_n \equiv v_n \frac{\partial v_n}{\partial r} = \frac{-2\delta^2 \dot{Q}^2}{r^5}, \quad (4.3)$$

$$\nu_n \Delta \mathbf{v}_n \equiv \nu_n \frac{1}{r^2} \frac{\partial}{\partial r} \left( r^2 \frac{\partial v_n}{\partial r} \right) = \frac{2\delta \nu_n \dot{Q}}{r^4}. \quad (4.4)$$

Then the absolute ratio is:

$$\left| \frac{(\mathbf{v}_n \cdot \nabla) \mathbf{v}_n}{\nu_n \Delta \mathbf{v}_n} \right| = \frac{\delta}{\nu_n r} \dot{Q}. \quad (4.5)$$

We see the ratio is linearly proportional to the power and inversely to the radius. In Figure 4.1 we plot the dependence of this ratio on the radius for three different heater powers.

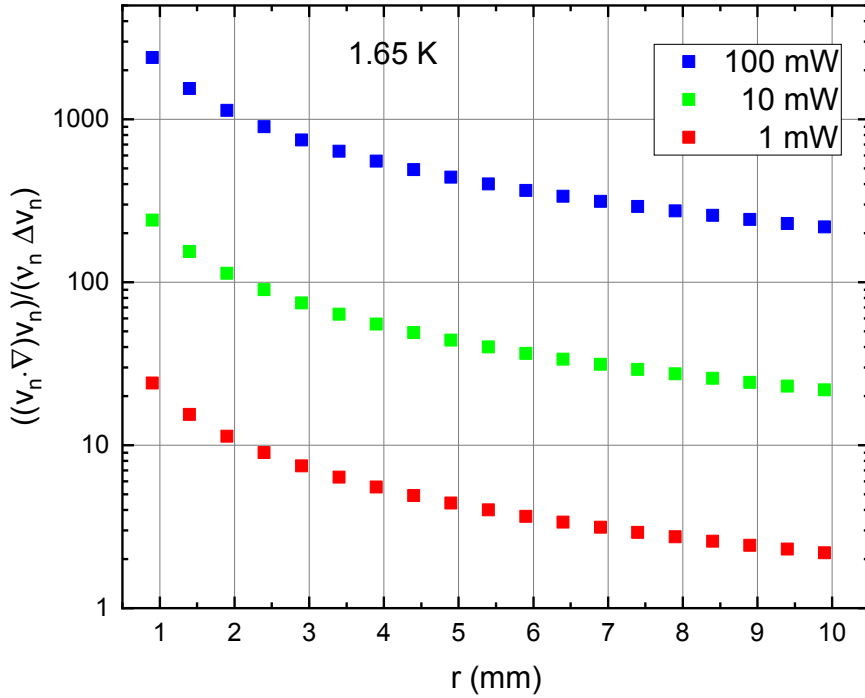


Figure 4.1: Ratio between the convective and diffusive term for the normal fluid velocity against the radial coordinate in the cell. For better comparison three powers were chosen, as indicated.

It is not simple to say when the flow undergoes instabilities and starts to possess turbulent structures, we would need a detailed analysis of the stability of this diverging flow. Currently we do not know of a theoretical work concerning

spherically diverging classical flow, since it is impossible to observe in nature due to the mass conservation law. So the most similar cases to ours are the studies of flow instability in diverging channels [29] or in submerged liquid jets [30, 31], which indicate diverging flows are less stable than, e.g., pipe flows or flows around a smooth body. Critical Reynolds numbers, based on the analysis in these works, range between 20 and 50. We note that our data correspond to a Reynolds number of around 40, when the transition to the second regime occurs, which seems consistent with these classical flows.

From Figure 4.1 it seems that at the power of 1 mW, we can assume the normal flow is turbulent only in the immediate vicinity of the heater, while in the rest of the cell, the flow is laminar. At the power of 10 mW, the highest ratio is around 350 near the heater, which can definitely lead to the emergence of significant turbulent structures, and in the rest of the cell the ratio is over 20. Hence it is possible that the turbulent region would not cover the entire cell. At the highest power of 100 mW, we can assume the flow is turbulent everywhere in the cell.

Looking at the figure 3.12 with VLD against power, we can propose the following model of turbulence in our cell.

- At the lowest powers up to 3 mW, the energy from the heater is mainly imposed into the excitation of quantised vortices (QV), leading to the increase of VLD. The effect of the normal flow is negligible, because it is mostly laminar, perhaps except very near the heater surface.
- At the middle powers between 3 mW and 30 mW, the energy is additionally consumed by the emergence of the classical-like turbulence in the normal component. This must lead to a lower energy input into QV and would cause the reduction of VLD growth as we observe it. The energy input into the classical-like flow would then propagate through the Richardson cascade and be eventually dissipated by viscosity.
- At powers higher than 30 mW, the energy is divided between the classical and quantum turbulence. Since the normal component is significantly turbulent in the whole cell, these highly turbulent structures can excite additional QV in the superfluid component not only at the heater surface but everywhere in the cell and so VLD may rise further. Conversely, quantum turbulence can also drive the classical one, but this would require a polarised (not random) vortex tangle.

This proposed mechanism stems from the idealized spherical thermal counterflow, i.e., from purely radially dependent velocity, but it is rather phenomenological, based on simple calculations and observations. To confirm this scenario, we would need either a direct experimental visualisation of the problem or a complex numerical simulation concerning the coupled dynamics of the classical continuum and the quantised vortices.

### 4.3 Local decay

We outline an explanation of the decay of the turbulent tangle in the spherical case. As we mentioned, the initial vortex tangle is not homogeneous and isotropic

as it is assumed by the Vinen equation 1.26. We assume, two competing effects exist, the first is the diffusion of vortices and the second is their local decay, which we expect to dominate, as shown by Milliken and Schwarz [32]. Any denser part of the vortex tangle should decay faster, since we know  $dL/dt \propto L^2$ . We will show, this spatially dependent (local) decay can explain the observed dependence  $L \propto 1/t$ . We will numerically solve a simple differential equation:

$$\frac{dL(r, t)}{dt} = -bL^2(r, t), \quad (4.6)$$

assuming the initial VLD is given by  $L(r, 0) = A/r^4$ . The time evolution is shown in Figure 4.2 and demonstrates that in the initial phase a rapid homogenization occurs, after which the turbulence decays as a homogeneous tangle.

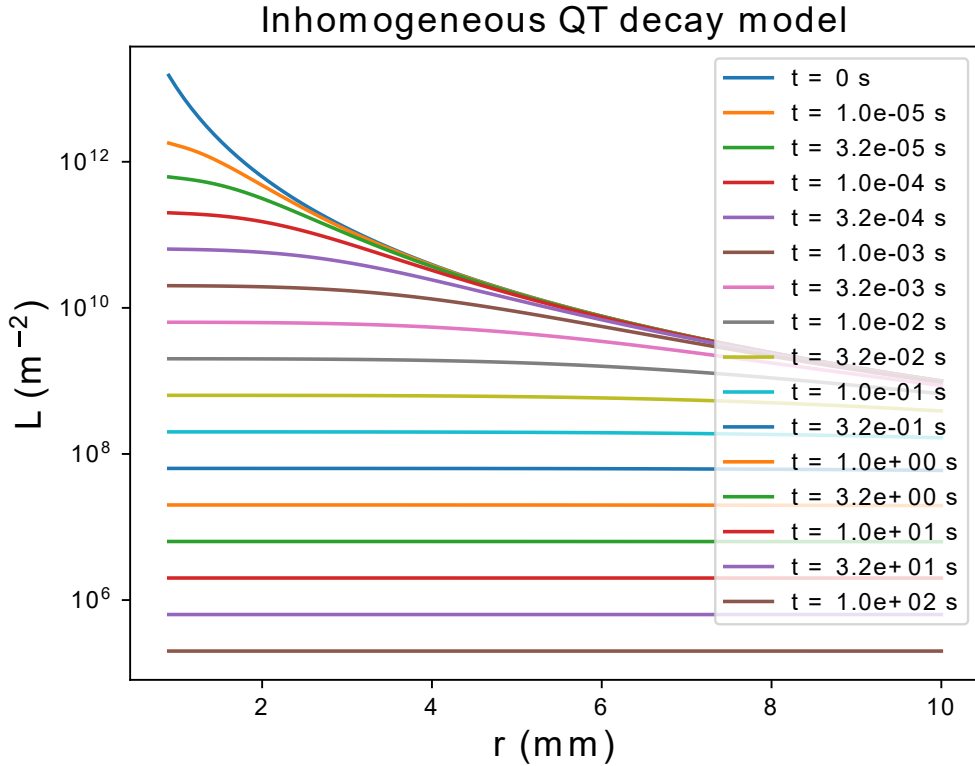


Figure 4.2: Numerical simulation of the decay of the vortex tangle in the spherical cell. Initial rapid homogenization is followed by a homogeneous decay, after less than 1 s.

From these results, the average VLD in the cell may be calculated, with weighting factors proportional to the volume of each spherical shell. We see in Figure 4.3 that the averaged VLD in the cell decays as  $1/t$  after the initial homogenization phase, which is in good agreement with the experimental observation.

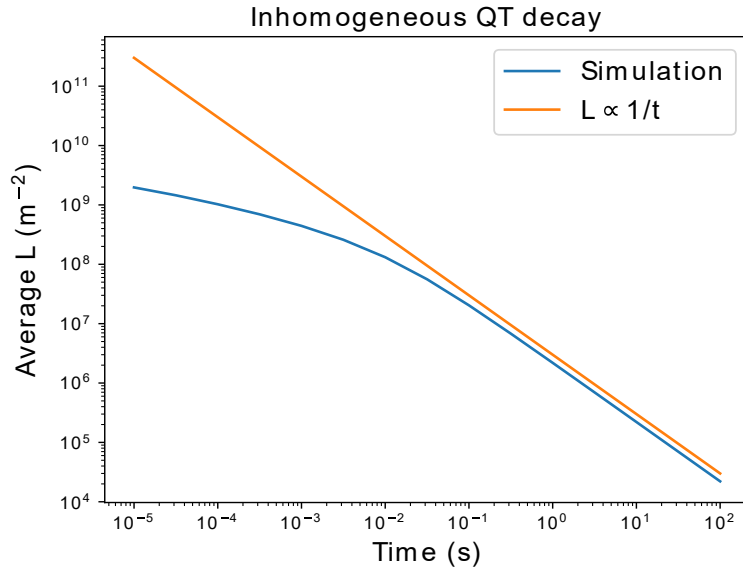


Figure 4.3: Result of the numerical solution of 4.6 with parameters  $A = 10^{13} \text{ m}^2$ ,  $b = -5 \cdot 10^{-8} \text{ m}^2/\text{s}$  and a dynamically adapted integration time step. We compare this result with the decay originating from the Vinen equation (1.26),  $L \propto 1/t$ .

## 4.4 Comparison to the thermal counterflow in channel

We can compare our results with those obtained in rectangular channels. The relevant measurements in channels were performed mainly by E. Varga resulting in his doctoral thesis [27] and publications [8],[28]. In the case of steady state turbulence, the data from the channels clearly follows the dependence  $L \propto v_{ns}^2$ , in stark contrast to our observations. We can point out the main differences between both cases. In the sphere,  $v_{ns} \propto 1/r^2$ , however in the channel  $v_{ns}$  is constant everywhere, since the area of the channel cross-section remains constant. This means that the longitudinal distribution of vortices is uniform. Also resonances in the channel are much simpler, having the profile of the sine function. Moreover, the solid boundaries are known to cause the transition to turbulence in the normal component in channel flows, and they can affect quantum turbulence as well, since quantized vortices can be caught or annihilate on them. On the other hand, we assume that the role of the outer boundary (inner wall of the cell) can be neglected in the spherical case, because  $v_{ns}$  is two orders of magnitude smaller here than at the heater.

In the case of turbulence decay, two types of decay were observed in channels. The Vinen type  $L \propto 1/t$  was present during the first second of the decay, then up to the finish of the decay the scaling  $L \propto t^{-3/2}$  was observed. This classical-like decay is again caused by the role of channel walls, which cause energy input at large scales due to the shear boundary layers. In the spherical geometry, this type of decay was not observed, supporting our interpretation that the role of the outer wall is not important and that turbulence is driven primarily at small scales comparable to the inter-vortex distance.



# Conclusion

In the following, we will summarise the results of this Thesis. The main goal was to specify and explain the peculiarities of the quantum turbulence driven by spherically symmetric thermal counterflow and compare our results to those previously obtained in rectangular channels.

We performed two completely independent measurements. The first was the measurement of the temperature profile caused by the He II flow, and the second was the measurement of VLD using the second sound attenuation method in both steady and decaying turbulence. To this end, we designed and manufactured the spherical brass cell.

- We mapped second sound resonances in the cell and compared them with calculations based on direct analytical solution of the Helmholtz equation or the numerical solution using spectral decomposition into vector spherical harmonics. The agreement between measured and calculated resonances is mainly apparent in the lower frequency range. At higher frequencies, resonances are significantly split due to their angular dependence. We chose two resonance frequencies for further measurements, 2950 Hz and 8923 Hz, and matched them to theoretically calculated values, which provides us with the knowledge of their profile in the cell.
- Next, we investigated the overheating of He II in the cell, which is caused by the thermal resistance of the body of the cell. We obtained that the temperature difference  $\Delta T$  between the temperature in the cell and in the bath is quadratic with the applied power, and the thermal resistance scales linearly. The highest value of  $\Delta T$  is 60 mK at 170 mW. The overheating can perturb our results at higher powers, since the resonance frequency shifts and the counterflow velocity is lower at higher temperatures, i.e., we can observe lower VLD than we would expect at the given temperature.
- The temperature profile measurement ran separately from the VLD measurements. We obtained reasonable agreement with the theory, which says the temperature falls with the radius from the heater as  $1/r^p$ , where  $p$  is between 5 and 6. The emergence of this profile is a direct consequence of the two-fluid behaviour of He II and is essential for steady state turbulence. Besides, it can affect the VLD profile and cause deviation from the ideal  $L \propto 1/r^4$ .
- Steady state turbulence was investigated at different temperatures using both resonance frequencies of second sound. We studied the dependence of Vortex line density (VLD) on the power applied to the heater. We found the counterflow velocity as the driving quantity for quantum turbulence, as expected. The observed dependence of VLD on  $\dot{Q}$  and  $v_{ns}$  does not coincide with what follows from the Vinen equation,  $L \propto v_{ns}^2$ , as in rectangular channels. On the other hand, we observed a distinct slowdown in the increase of VLD at medium powers and velocities. We proposed a phenomenological explanation concerning the effect of classical-like turbulence in the normal component. The observed turbulence in the normal component is in a sense

unique, since the flow is diverging in all directions, and  $v_n$  is the function of radius. This has no direct analogy in classical fluid dynamics. We hypothesize that this flow may become unstable, and produce turbulence.

- We also evaluated the  $\gamma$ -factor in our cell and compared it with that observed in channels. The  $\gamma$ -factor should be constant at the given temperature, but we observe this only at really small  $v_{ns}$ . This is caused by the specifics of the spherical geometry, when in contrast to the channel, our turbulence is less affected by the presence of walls.
- The turbulence decay was investigated at multiple applied powers and bath temperatures. Despite small deviations at early and late times, we observed the decay predicted by the Vinen equation,  $L \propto 1/t$ . This indicates that the turbulence is driven mostly at small scales. However, the Vinen equation assumes a homogeneous vortex tangle, which is not initially fulfilled by the VLD profile in our cell. We assume that homogenization of this vortex tangle occurs after the heater is switched off, thanks to the predominantly local decay. We see different behaviour than in channels, where also the decay derived from Kolmogorov theory  $L \propto t^{-3/2}$  is seen.

The author should emphasize that this work is a direct extension of his Bachelor's thesis. In this work, we used a newly manufactured metal cell, we have fully described the spherical resonances, revised the interpretation of VLD dependence on  $v_{ns}$  and measured the temperature profile in the cell. For a more complete understanding of this phenomenon, we would need appropriate numerical calculations or visualization experiments, which should be the next step of our research.

# Bibliography

- [1] F. London. The  $\lambda$ -phenomenon of liquid helium and the bose-einstein degeneracy. *Nature*, 141:643–644, 1938.
- [2] L. Tisza. Transport phenomena in helium ii. *Nature*, 141:913, 1938.
- [3] L. Landau. Theory of the superfluidity of helium ii. *Phys. Rev.*, 60:356–358, 1941.
- [4] R. P. Feynmann. Application of quantum mechanics to liquid helium. *Progress in Low Temperature Physics*, 1:17–53, 1955.
- [5] E. J. Yarmchuk and R. E. Packard. Photographic studies of quantized vortex lines. *J Low Temp Phys*, 46:479–515, 1982.
- [6] G. Bewley, D. Lathrop, and K. Sreenivasan. Visualization of quantized vortices. *Nature*, 441:588, 2006.
- [7] L. Skrbek, D. Schmoranzler, Š. Midlik, and K. R. Sreenivasan. Phenomenology of quantum turbulence in superfluid helium. *Proceedings of the National Academy of Sciences*, 118(16), 2021.
- [8] E. Varga, S. Babuin, and L. Skrbek. Second-sound studies of coflow and counterflow of superfluid  $^4\text{He}$  in channels. *Physics of Fluids*, 27:065101, 2015.
- [9] S. Inui and M. Tsubota. Spherically symmetric formation of localized vortex tangle around a heat source in superfluid  $^4\text{He}$ . *Phys. Rev. B*, 101:214511, 2020.
- [10] E. Varga. Peculiarities of spherically symmetric counterflow. *J Low Temp Phys*, 196:28–34, 2019.
- [11] Y. A. Sergeev and C. F. Barenghi. Turbulent radial thermal counterflow in the framework of the HVBK model. *EPL (Europhysics Letters)*, 128:26001, 2019.
- [12] E. Rickinson, C. F. Barenghi, Y. A. Sergeev, and A. W. Baggaley. Superfluid turbulence driven by cylindrically symmetric thermal counterflow. *Phys. Rev. B*, 101:134519, 2020.
- [13] S. B. Pope. *Turbulent Flows*. 10th printing. Cambridge University Press, 2013.
- [14] L. D. Landau and E. M. Lifshitz. *Fluid Mechanics*. Second edition. Pergamon Press, 1987.
- [15] A. N. Kolmogorov. Dissipation of energy in locally isotropic turbulence. *Dokl. Akad. Nauk SSSR*, 32:19–21, 1941.
- [16] R. J. Donnelly and C. F. Barenghi. The observed properties of liquid helium at the saturated vapour pressure. *Journal of Physical and Chemical Reference Data*, 27:1217–1274, 1998.

- [17] D. R. Tilley and J. Tilley. *Superfluidity and Superconductivity*. Adam Hilger Ltd, 1986.
- [18] C. F. Barenghi and Parker N. G. *A Primer on Quantum Fluids*. Springer, Cham, 2016.
- [19] W. F. Vinen. Mutual friction in a heat current in liquid helium ii iii. theory of the mutual friction. *Royal Society*, 242(1231):493–515, 1957.
- [20] K. W. Schwarz. Three-dimensional vortex dynamics in superfluid  $^4\text{He}$ : Homogeneous superfluid turbulence. *Phys. Rev. B*, 38:2398–2417, 1988.
- [21] Z. Xie, Y. Huang, F. Novotný, et al. Spherical thermal counterflow of he ii. *J Low Temp Phys*, 2022.
- [22] L. Skrbek et al. *Fyzika nízkých teplot, I. část*. MATFYZPRESS, 2011.
- [23] S. Babuin, M. Stammeier, E. Varga, et al. Spherical thermal counterflow of he ii. *J Low Temp Phys*, 2012.
- [24] D. D. Holm. Introduction to hvbk dynamics. *Quantized Vortex Dynamics and Superfluid Turbulence*, Springer Berlin Heidelberg, pages 114–130, 2001.
- [25] F. Pobell. *Matter and Methods at Low Temperatures*. Springer, 2007.
- [26] S. W. Van Sciver. *Helium Cryogenics*. Second Edition. Springer, 2012.
- [27] E. Varga. *Experimental and numerical investigation of quantum turbulence in He II*. PhD thesis, Charles University, 2018.
- [28] E. Varga and L. Skrbek. Dynamics of the density of quantized vortex lines in counterflow turbulence: Experimental investigation. *Phys. Rev. B*, 97:064507, 2018.
- [29] G. Swaminathan et al. Global instabilities in diverging channel flows. *Theor. Comput. Fluid Dyn.*, 25:53–64, 2011.
- [30] V. Shtern and F. Hussain. Effect of deceleration on jet instability. *Journal of Fluid Mechanics*, 480:283–309, 2003.
- [31] P. J. Morris. The spatial viscous instability of axisymmetric jets. *Journal of Fluid Mechanics*, 77:511–529, 1976.
- [32] F. P. Millikent and K. W. Schwarz. Free decay of superfluid turbulence. *Phys. Rev. Letters*, 48(17):1204–1207, 1982.

# A. Attachments

## A.1 Attachment 1. Spherical Thermal Counterflow of He II



# Spherical Thermal Counterflow of He II

Zhuolin Xie<sup>1</sup> · Yunhu Huang<sup>1</sup> · Filip Novotný<sup>1</sup> · Šimon Midlik<sup>1</sup> · David Schmoranzer<sup>1</sup> · Ladislav Skrbek<sup>1</sup>

Received: 30 September 2021 / Accepted: 23 January 2022

© The Author(s), under exclusive licence to Springer Science+Business Media, LLC, part of Springer Nature 2022

## Abstract

Past investigations of thermal counterflow in He II were mostly conducted in pipes/channels of constant cross-sections, which are often unduly influenced by the presence of walls. We devise and carry out an experiment using a spherically symmetric setup to study unbounded counterflow in order to gain better understanding of interactions between quantized vortices and counterflow; the preliminary analysis shows that this method is viable.

**Keywords** Superfluid · Counterflow · Vortex · Spherical

## 1 Heat transport in superfluid <sup>4</sup>He

Heat transport in superfluid <sup>4</sup>He (He II) differs from that in classical viscous fluids in that He II at  $T \gtrsim 1$  K can be described as a mixture of two components, the superfluid component and the normal one; the total density is the sum of the two component densities  $\rho = \rho_s + \rho_n$  [1]. In the past, thermal counterflow of He II had frequently been studied in pipes and channels of constant cross-sections [2–5, 10], typically by applying a heat flux  $\dot{q}$  to the dead end of the channel with the other end open to the helium bath.

For small  $\dot{q}$ , the flow of the normal fluid is laminar, and there are no quantized vortices in the potential flow of the superfluid component except, in practice, of few remnant vortices due to surface roughness of the channel walls. The normal and superfluid velocity fields are nearly independent, and a constant temperature gradient along the channel is established. Upon increasing  $\dot{q}$  thermal counterflow becomes turbulent. In some cases, a tangle of quantized vortex lines becomes generated in the superfluid while the normal fluid remains laminar, forming so-called

---

✉ Yunhu Huang  
yunhu.huang@gmail.com

<sup>1</sup> Faculty of Mathematics and Physics, Charles University, Ke Karlovu 3, Prague 121 16, Czech Republic

TI state of counterflow turbulence [6]. Further increase in heat flux causes the flow to enter the TII state,<sup>1</sup> where both components are turbulent [7, 8]. The presence of the ångström-sized vortex lines couples the normal and superfluid velocity fields by an effective mutual friction force  $\mathbf{F}_{\text{ns}}$  arising from phonons and rotons scattering off the vortices. Each vortex carries one quantum of circulation  $\kappa = h/m_4 \approx 9.97 \times 10^{-8} \text{m}^2/\text{s}$ , where  $h$  is the Planck's constant, and  $m_4$  denotes the mass of a  $^4\text{He}$  atom [9].

Since the pioneering work of Vinen [2–5], many experimental, theoretical and numerical studies followed. Despite these efforts, many aspects of counterflow turbulence are still not well understood. One reason for the difficulty is that, due to its quantum nature, turbulent thermal counterflow of He II is more complex than classical viscous fluid flow in pipe or channels [10], and various aspects of bulk counterflow and the influence of channel walls are generally very difficult to disentangle.

A possibility to overcome this obstacle is to study unbounded thermal counterflow, thus eliminating the influence of walls. The main idea for the present work follows the first theoretical and numerical study of spherically symmetric counterflow by Varga [11], the subsequent work of Inui and Tsubota [12], as well as the 2D cylindrically symmetric studies of the Newcastle group [13, 14]. We expect the spherical symmetry to confine the direction of counterflow, and consequently of the vortex line density gradient, to be essentially in the radial direction, such that we may avoid the complications arising near boundaries. Here we report the design and working progress of an experiment studying turbulent 3D thermal counterflow of He II in a spherical cell, generated by a small heater and probed by second sound attenuation [15]. Additionally, we discuss our companion experiment where the temperature gradient in 3D counterflow [16] is directly measured using sensitive thermometry.

## 2 Spherical counterflow

Heat transport in He II follows the empirical relationship  $\nabla T = -f(T)\dot{q}^{3.4}$ , where  $f(T)$  can be viewed as a generalized conductivity [17, 18]. This agrees<sup>2</sup> with recent measurements performed directly in the bulk liquid for turbulent thermal counterflow in a channel of rectangular cross-section of 7 mm side [16]. Macroscopically, temperature gradient  $\nabla T$  and vortex line density  $L$  are related by Hall-Vinen-Bekarevich-Khalatnikov (HVBK) equations and described by [16, 19]

$$\rho_n \frac{D\mathbf{u}_n}{Dt} = -\frac{\rho_n}{\rho} \nabla p + \eta_n \Delta \mathbf{u}_n - \rho_s \sigma \nabla T + \mathbf{F}_{\text{ns}}, \quad (1a)$$

<sup>1</sup> Additionally, in rectangular channels of high (1:10) aspect ratio with the small dimension less than 100  $\mu\text{m}$ , only one transition has been observed, denoted by Tough as T III [6].

<sup>2</sup> Except within a thin boundary layer adjacent to the heater, physical origin of which is not yet fully understood [16]

$$\rho_s \frac{D\mathbf{u}_s}{Dt} = -\frac{\rho_s}{\rho} \nabla p + \rho_s \sigma \nabla T - \mathbf{F}_{ns}, \quad (1b)$$

where  $D\mathbf{u}/Dt \equiv \partial\mathbf{u}/\partial t + (\mathbf{u}\nabla)\mathbf{u}$ , and  $p$ ,  $\sigma$ ,  $\eta_n$  and  $\mathbf{F}_{ns}$  are, respectively, the pressure, the specific entropy, the normal fluid dynamic viscosity and the mutual friction force. The latter can be written in a simplified form as [9]

$$\mathbf{F}_{ns} = -\alpha\kappa\rho_s L(\mathbf{u}_n - \mathbf{u}_s), \quad (2)$$

where  $\alpha$  is the tabulated dissipative mutual friction parameter [20]. The vortex line density is related to counterflow velocity  $u_{ns}$  by

$$L = \gamma^2(u_{ns} - u_c)^2 \approx \gamma^2 u_{ns}^2, \quad (3)$$

where  $\gamma$  is a temperature dependent parameter known within the accuracy of about 20%, while  $u_c$  is the critical velocity typically of the order of 1 mm/s.

For spherically symmetric heat flow, Eq. 1 reduce to the 1D case

$$\rho\sigma \frac{\partial T}{\partial r} = -\frac{\rho_n}{2} \frac{\partial}{\partial r} \left[ u_n^2 \left( 1 - \frac{\rho_n^2}{\rho_s^2} \right) \right] + \eta_n \left( \frac{1}{r^2} \frac{\partial}{\partial r} r^2 \frac{\partial u_n}{\partial r} - \frac{2u_n}{r^2} \right) - \alpha\kappa\gamma^2 \frac{\rho^4}{\rho_s^3} u_n^3. \quad (4)$$

At a distance  $r$  from the center, in the steady-state, the heat supply  $\dot{Q}$  is carried away by the normal fluid alone:  $\dot{Q} = 4\pi r^2 \rho\sigma T u_n$ , which, when substituted into Eq. 4, enables us to numerically calculate the temperature gradient.

It is instructive, however, to examine the approximate analytical solution. Assuming that the first two terms on the right-hand side of Eq. 4 are typically negligible (the validity of which can be corroborated by the result of this very calculation) and that the resulting temperature gradient is small, we obtain

$$T(r) = \frac{\alpha\kappa\gamma^2}{5\sigma^4\rho_s^3} \left( \frac{\dot{Q}}{4\pi T} \right)^3 \frac{1}{r^5} + T_0, \quad (5)$$

where  $T_0$  is the bath temperature at infinity. This approximation is sufficiently accurate when compared to the result of full numerical calculation of Eq. 4 under our experimental conditions, i.e., when  $\dot{Q}$  is of the order of 100 mW and the distance  $r$  varies from millimeters to centimeters.

### 3 Temperature profile measurement

We separately conducted a complementary experiment to directly measure the temperature distribution surrounding the spherical heater. The setup is shown in Fig. 1. The main body is a hollow frame, 3D printed using the copper-doped PLA filament. The spherical heater  $\sim 2$  mm in diameter is made of a surface-mount device resistor encased in Stycast and silver epoxy, suspended from a thin tube which houses the heater leads. The upper end of the tube is connected to the driving shaft of a precision linear motor, thus the heater assembly can be moved in the vertical direction

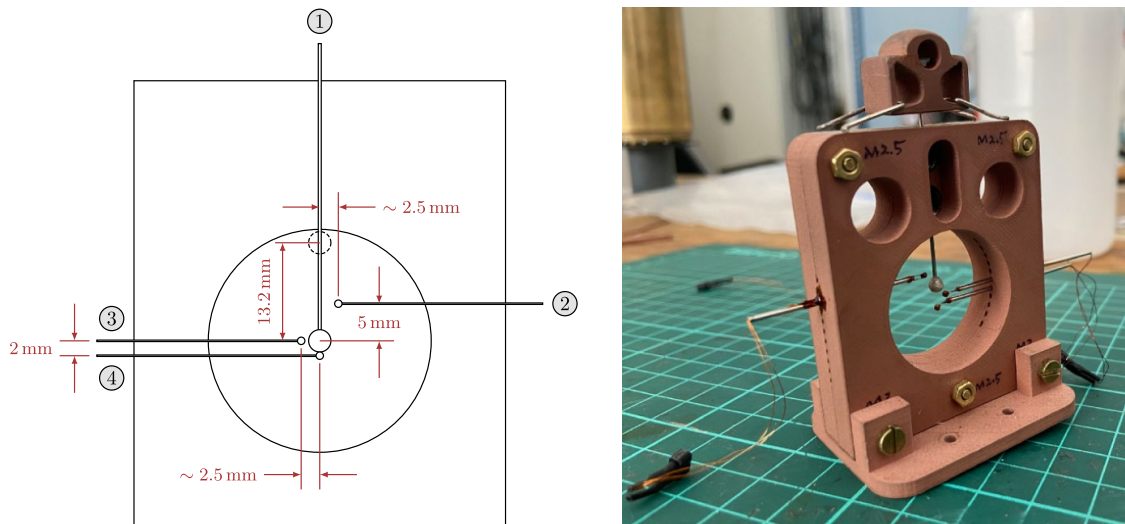


**Fig. 1** Schematic diagram and photograph of the temperature profile measurement setup. Labels in the diagram denote the connection to the linear motor (1); and to the TTRG thermometers (2–4) (Color figure online)

freely within its range of travel  $\sim 13$  mm. Three TTRG thermometers [21–23] are  $\sim 0.5$  mm in size and are mounted on the sides of the frame such that when the heater travels along its vertical path, each thermometer will be as close as  $\sim 0.1$  mm to the heater surface.

The entire setup is then put into the helium bath with its temperature controlled using a pumping unit consisting of a Roots pump and a mechanical backing pump. We apply power ranging from 200 mW to 660 mW to the heater at temperatures from 1.25 K to 2 K. For each power and temperature, the heater was set at multiple vertical positions and readings of all three thermometers were recorded, all automated by a custom LabView program. Thus, we obtain the relation between the temperature change at each thermometer and its distance from the heater, from where we can deduce the temperature profile around a stationary heater.

Preliminary analysis (e.g., Fig. 2) shows that the measured temperature profiles agree with the formulation given in the previous section. In particular, if  $r \gtrsim 2$  mm or the heater power is below  $\lesssim 200$  mW, Eq. 5 is sufficient in describing the temperature profile; only when both these conditions are violated do we need to resort to the full numerical solution of Eq. 4. These measurements indicate that in our main experiment (see the next section) we should expect the temperature rise outside the heater up to a few mK.

## 4 Main experimental setup

Our main experimental cell is a 3D-printed regular dodecahedron surrounding a spherical cavity  $\sim 16$  mm in diameter that contains He II. A small spherical resistive heater  $\sim 1.8$  mm in diameter is placed in the center, suspended by a cylindrical holder with a diameter of  $\sim 1$  mm (see Fig. 3). On each of the remaining eleven flat outer surfaces, a circular hole is cut such that a circular second sound transducer

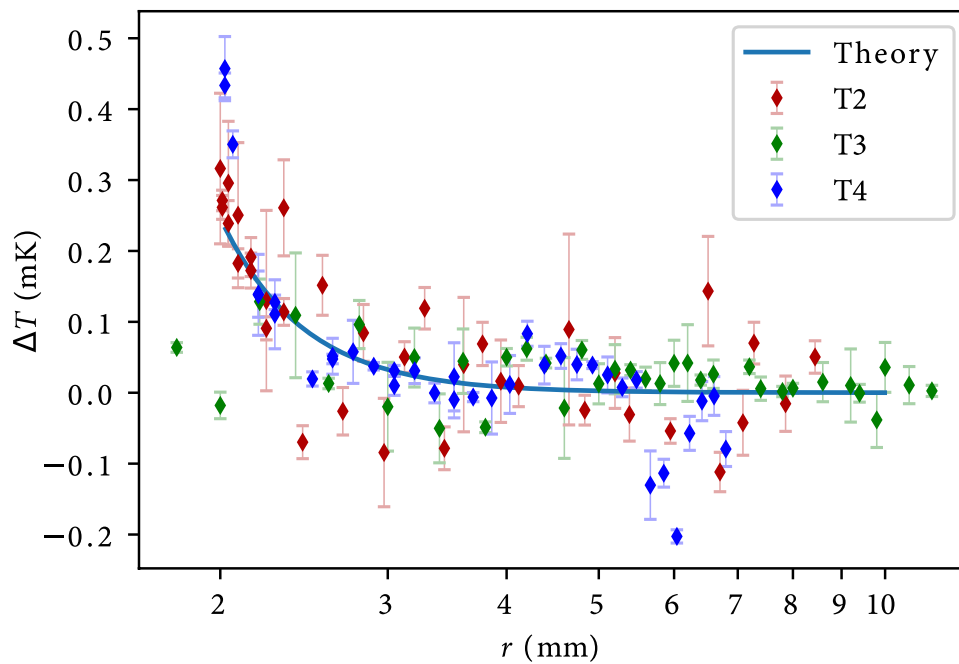


**Fig. 2** The difference between the local temperature (measured using thermometers No 2, 3 and 4 shown in Fig. 1) and the bath temperature stabilized to  $T = 1.5\text{K}$ , plotted together with the numerically calculated temperature gradient (Eq. 4) versus the distance from center of the heater, powered by 500mW. The data points are highly scattered, likely due to noise; some of them might be rejected based on pending further analysis (Color figure online)

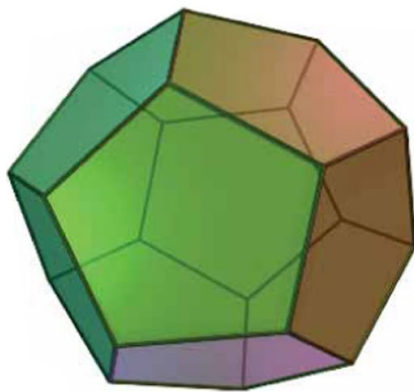


**Fig. 3** Experimental cell is of the form of a regular dodecahedron outside (left) containing a nearly spherical sample of liquid helium inside. The photograph shows the cell with second sound transducers attached and the spherical heater in its center (Color figure online)

9 mm in diameter can be mounted in it. Each transducer consists of a brass cylinder connected to an electrode, with a thin micro-pore membrane attached on its inward face. The membrane is coated with a thin layer ( $\sim 30\text{nm}$ ) of gold on the side facing away from the electrode. The second sound attenuation technique is described in detail in Refs. [15, 24].

The cell is affixed onto a cryogenic insert in a cylindrical helium bath (diameter  $\sim 200\text{mm}$ ). The temperature of the bath is lowered and stabilized using a pumping

unit consisting of a Roots pump and a mechanical backing pump, with a PID regulation loop using a resistive heater for fine control. Vapour pressure of the bath is monitored by the MKS Baratron, and additional calibrated resistive thermometers [21–23] are installed at various locations inside the bath and measured by the Lake-Shore 336 temperature controller.

The heater is a small  $\sim 50 \Omega$  resistor encased in a Stycast 2850 sphere, as seen in the photograph in Fig. 3. It is driven by a DC voltage using a Keithley power supply and generates a nearly spherical counterflow. For the present experiment, we installed two second sound transducers diametrically opposing each other, one as the sound source driven by an AC signal from the Agilent 33220A function generator, the other as the second sound sensor monitored by the Stanford Research SR830 lock-in amplifier.

We performed measurements at various bath temperatures using different heater powers. At each temperature, with heater power off, we swept the frequency of the driving voltage on the second sound driver and measured the response from the sensor, locating the second sound resonance frequencies. Then, after fixing the drive at a chosen resonance frequency and the sensor being constantly monitored, we swept the heater power within a preset range, and the sensor signal amplitude was recorded as a function of power. We ensured that heater power stopped at each set value for sufficiently long time so that the temperature and vortex line density inside the cell had settled to steady-state distributions. Each amplitude  $A$  so measured can be compared to the amplitude without the heater  $A_0$  and used to infer the vortex line density inside the cell.

To obtain the vortex line density  $L$ , we need accurate knowledge of the second sound waves inside the cell. Although similar experiments have been performed and analyzed in rectangular channels [15, 16, 24], we are still in the process of finalizing the numerical methods for the spherical geometry, therefore the detailed analysis will be available in a later paper. Meanwhile, however, we do have approximate solutions for second sound in a sphere.

## 5 Second sound in a spherical cell

Neglecting dissipative phenomena, the second sound wave can be described in terms of a scalar potential  $\Phi$ , with the counterflow velocity given as  $\mathbf{u}_{\text{ns}} = \nabla\Phi$ . Assuming small temperature variations,  $\Phi$  satisfies the standard wave equation  $\nabla^2\Phi = c^{-2}\partial^2\Phi/\partial t^2$ , where  $c = c(T)$  is the second sound velocity. As our cell is spherical, we seek the radial modes of standing waves, thus

$$\frac{1}{r^2} \frac{\partial}{\partial r} \left( r^2 \frac{\partial \Phi}{\partial r} \right) = \frac{1}{c^2} \frac{\partial^2 \Phi}{\partial t^2}.$$

Separating variables, by letting  $\Phi \equiv R(r)T(t)$ , leads to

$$\frac{1}{Rr^2} \frac{\partial}{\partial r} \left( r^2 \frac{\partial R}{\partial r} \right) = \frac{1}{Tc^2} \frac{\partial^2 T}{\partial t^2} \equiv C \quad (6)$$

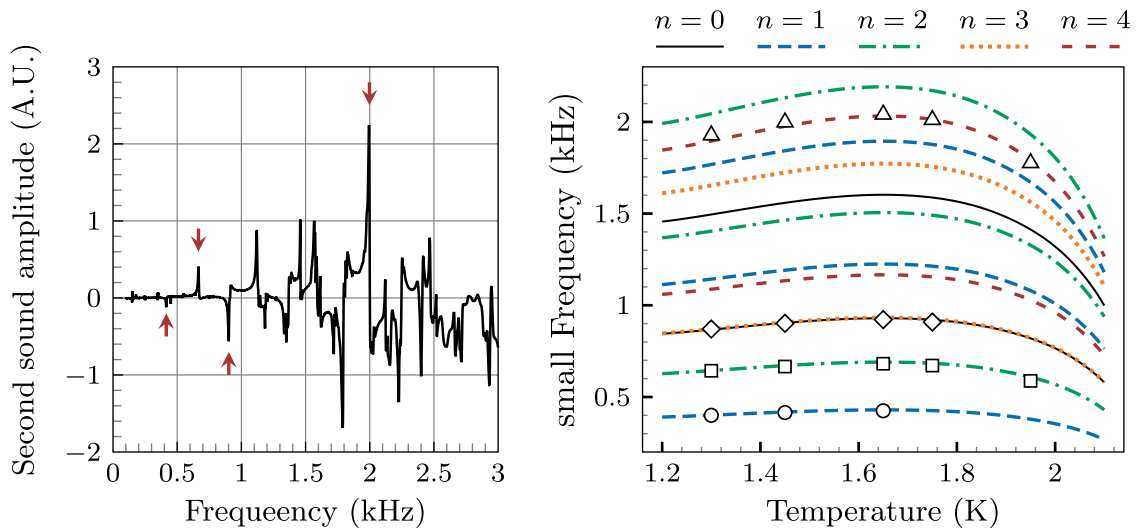


**Fig. 4** Left: An example of the second sound sensor response to the frequency sweep with the heater off, at  $T = 1.45$  K. The arrows mark the resonance frequencies chosen for subsequent attenuation measurements. Right: The second sound resonance frequencies calculated based on spherical Bessel functions plotted versus the temperature, in comparison with those measured. The legend denotes the order number,  $n$ , of the spherical Bessel function (Color figure online)

for some constant  $C$ . The eigen-solutions to the above equations are

$$R(r) = \alpha_n j_n(kr) + \beta_n y_n(kr), \quad (7)$$

$$T(t) = a \cos(ckt) + b \sin(ckt), \quad (8)$$

$$C = -k^2, \quad (9)$$

where  $j_n$  and  $y_n$  are the  $n$ th order spherical Bessel and Neumann functions, respectively. The equations are coupled through the wave vector  $k$ .

The solution domain is limited between two spherical surfaces, the inner one at the heater surface with radius  $r_0$ , and the outer one at the cell wall with radius  $r_1$ . A standing wave solution requires the sound amplitude to be zero at the boundaries, meaning  $\partial R/\partial r = 0$  at  $r = r_0$  and  $r = r_1$ . Therefore, for there to be a resonance at some wave vector  $k$  of mode  $n$ , there must exist values  $\alpha_n$  and  $\beta_n$  such that

$$\alpha_n j'_n(kr_0) + \beta_n y'_n(kr_0) = 0, \quad \alpha_n j'_n(kr_1) + \beta_n y'_n(kr_1) = 0.$$

Here we used  $j'$  and  $y'$  to indicate spatial derivatives for brevity. For every given mode number  $n$ , multiple solutions for  $k$  can be obtained numerically. Each  $m$ th root of the  $n$ th mode,  $k_{n,m}$ , corresponds to a resonance frequency  $f_{n,m} = ck_{n,m}/2\pi$ . Note that solutions of  $k$  depend on geometry but not temperature. The frequency of the same resonance mode varies with temperature only through  $c = c(T)$ . In other words, all the curves in Fig. 4 have the same shape except for being scaled differently in the vertical direction.

This calculation enables us to compare the measured resonance frequencies against the theoretically predicted values. They match well, as shown in Fig. 4.

## 6 Conclusions

We have generated spherically symmetric thermal counterflow and verified the method of probing it by second sound attenuation inside a spherical cell surrounding a spherical heater placed in its center. Additionally, we have performed an accompanying experiment and directly measured the temperature gradient outside a spherical heater in open He II bath. The results of both experiments qualitatively confirm our model of thermal counterflow in spherical geometry. The ongoing detailed analysis should enable better knowledge of the vortex line distribution inside the cell and provide new insights into the generation, transportation and annihilation of quantized vortices in unbounded spherical thermal counterflow of He II.

The authors thank E. Varga for stimulating discussions and help at the early part of this project and acknowledge the support by the Czech Science Foundation under Project GAČR 20-00918S.

## References

1. C.F. Barenghi, L. Skrbek, K.R. Sreenivasan, Introduction to quantum turbulence. *Proc. Natl. Acad. Sci. U.S.A.* **111**, 4649 (2014)
2. W.F. Vinen, Mutual friction in a heat current in liquid helium II, I. Experiments on steady heat currents. *Proc. R. Soc. A* **240**, 114 (1957)
3. W.F. Vinen, Mutual friction in a heat current in liquid helium II, II. Experiments on transient effects. *Proc. R. Soc. A* **240**, 128 (1957)
4. W.F. Vinen, Mutual friction in a heat current in liquid helium II, III. Theory of the mutual friction. *Proc. R. Soc. A* **242**, 493 (1957)
5. W.F. Vinen, Mutual friction in a heat current in liquid helium II, IV. Critical heat currents in wide channels. *Proc. R. Soc. A* **243**, 400 (1958)
6. J. T. Tough, *Superfluid turbulence*, in *Progress in Low Temperature Physics* (North-Holland Publ. Co., , Vol. VIII (1982)
7. A. Marakov, J. Gao, W. Guo, S.W. VanSciver, G.G. Ihas, D.N. Mc Kinsey, W.F. Vinen, Visualization of the normal-fluid turbulence in counterflowing superfluid He-4. *Phys. Rev. B* **91**, 094503 (2015)
8. J. Gao, E. Varga, W. Guo, W.F. Vinen, Energy spectrum of thermal counterflow turbulence in superfluid helium-4. *Phys. Rev. B* **96**, 094511 (2017)
9. R.J. Donnelly, *Quantized Vortices in Helium II* (Cambridge University Press, Cambridge, 1991)
10. L. Skrbek, D. Schmoranzler, Š Midlik, K.R. Sreenivasan, Phenomenology of quantum turbulence in superfluid helium. *Proc. Nat. Acad. Sci. USA* **118**, e2018406118 (2021)
11. E. Varga, Peculiarities of spherically symmetric counterflow. *J. Low Temp. Phys.* **196**, 28 (2019)
12. S. Inui, M. Tsubota, Spherically symmetric formation of localized vortex tangle around a heat source in superfluid  $^4\text{He}$ . *Phys. Rev. B* **101**, 214511 (2020)
13. E. Rickinson, C.F. Barenghi, Y.A. Sergeev, A.W. Baggaley, Superfluid turbulence driven by cylindrically symmetric thermal counterflow. *Phys. Rev. B* **101**, 134519 (2020)
14. Y.A. Sergeev, C.F. Barenghi, Turbulent radial thermal counterflow in the framework of the HVBK model. *Europhys. Lett.* **128**, 26001 (2019)

15. E. Varga, M.J. Jackson, D. Schmoranzer, L. Skrbek, The use of second sound in investigations of quantum turbulence in He II. *J. Low Temp. Phys.* **197**, 130 (2019)
16. E. Varga, L. Skrbek, Thermal counterflow of superfluid He-4: temperature gradient in the bulk and in the vicinity of the heater. *Phys. Rev. B* **100**, 054518 (2019)
17. A. Sato, M. Maeda, and Y. Kamioka, in *Proceedings of the Twentieth International Cryogenic Engineering Conference (ICEC20)*, edited by L. Zhang, L. Lin, and G. Chen (Elsevier Science, Oxford, 2005), Chap. 201, pp. 849-852
18. S.W. Van Sciver, *Helium Cryogenics* (Springer, New York, 2012)
19. J.D. Henberger, J.T. Tough, *Phys. Rev. B* **25**, 3123 (1982)
20. R.J. Donnelly, C.F. Barenghi, *J. Phys. Chem. Ref. Data* **27**, 1217 (1998)
21. <http://microsensor.com.ua>
22. V.F. Mitin, P.C. McDonald, F. Pavese, N.S. Boltovets, V.V. Kholevchuk, IYu. Nemish, V.V. Basanets, V.K. Dugaev, P.V. Sorokin, R.V. Konakova, E.F. Venger, E.V. Mitin, *Cryogenics* **47**, 474 (2007)
23. V.F. Mitin, V.V. Kholevchuk, B.P. Kolodych, *Cryogenics* **51**, 68 (2011)
24. S. Babuin, M. Stammeier, E. Varga, M. Rotter, L. Skrbek, *Phys. Rev. B* **86**, 134515 (2012)

**Publisher's Note** Springer Nature remains neutral with regard to jurisdictional claims in published maps and institutional affiliations.